The Astrophysical Journal, 747:52 (21pp), 2012 March 1 doi:10.1088/0004-637X/747/1/52

RESOLVING THE LUMINOSITY PROBLEM IN LOW-MASS STAR FORMATION

Michael M. Dunham[1] and Eduard I. Vorobyov[2,3]
[1] Department of Astronomy, Yale University, P.O. Box 208101, New Haven, CT 06520, USA; michael.dunham@yale.edu
[2] Institute of Astronomy, The University of Vienna, Vienna 1180, Austria; eduard.vorobiev@univie.ac.at
[3] Institute of Physics, Southern Federal University, Stachki 194, Rostov-on-Don 344090, Russia
Received 2011 September 20; accepted 2011 December 19; published 2012 February 14

ABSTRACT

We determine the observational signatures of protostellar cores by coupling two-dimensional radiative transfer calculations with numerical hydrodynamical simulations that predict accretion rates that both decline with time and feature short-term variability and episodic bursts caused by disk gravitational instability and fragmentation. We calculate the radiative transfer of the collapsing cores throughout the full duration of the collapse, using as inputs the core, disk, protostellar masses, radii, and mass accretion rates predicted by the hydrodynamical simulations. From the resulting spectral energy distributions, we calculate standard observational signatures ($L_{\rm bol}$, $T_{\rm bol}$, $L_{\rm bol}/L_{\rm smm}$) to directly compare to observations. We show that the accretion process predicted by these models reproduces the full spread of observed protostars in both $L_{\rm bol}$–$T_{\rm bol}$ and $L_{\rm bol}$–$M_{\rm core}$ space, including very low luminosity objects, provides a reasonable match to the observed protostellar luminosity distribution, and resolves the long-standing luminosity problem. These models predict an embedded phase duration shorter than recent observationally determined estimates (0.12 Myr versus 0.44 Myr), and a fraction of total time spent in Stage 0 of 23%, consistent with the range of values determined by observations. On average, the models spend 1.3% of their total time in accretion bursts, during which 5.3% of the final stellar mass accretes, with maximum values being 11.8% and 35.5% for the total time and accreted stellar mass, respectively. Time-averaged models that filter out the accretion variability and bursts do not provide as good of a match to the observed luminosity problem, suggesting that the bursts are required.

Key words: hydrodynamics – ISM: clouds – radiative transfer – stars: formation – stars: low-mass – stars: protostars

Online-only material: color figures

1. INTRODUCTION

Low-mass stars form from the gravitational collapse of dense cores of gas and dust (e.g., Beichman et al. 1986; Di Francesco et al. 2007; Ward-Thompson et al. 2007a). In the simplest model, the collapse of a singular isothermal sphere initially at rest as first considered by Shu (1977) and later extended by Terebey et al. (1984, hereafter TSC84) to include rotation (often called the "standard model" of star formation), collapse proceeds in an "inside-out" fashion, beginning in the center of the core, moving outward at the sound speed, and giving rise to a constant mass accretion rate of $\sim 2 \times 10^{-6}\ M_{\odot}\ {\rm yr}^{-1}$. Many modifications to this model have been explored, including non-zero initial inward motions (Larson 1969; Penston 1969; Hunter 1977; Fatuzzo et al. 2004), magnetic fields (Galli & Shu 1993a, 1993b; Li & Shu 1997; Basu 1997), isothermal spheres that are *not* singular but feature flattened density profiles at small radii (Foster & Chevalier 1993; Henriksen et al. 1997), and a finite outer boundary (Henriksen et al. 1997; Vorobyov & Basu 2005a). All but the latter (finite outer boundary) generally increase the accretion rate over that predicted by the standard model.

A significant shortcoming of the standard model is the classic "luminosity problem," whereby accretion at the above rate produces accretion luminosities ($L_{\rm acc} \propto M_{*}\dot{M}$) factors of 10–100 higher than typically observed for embedded protostars. First noticed by Kenyon et al. (1990) and further investigated by Kenyon et al. (1994) and Kenyon & Hartmann (1995), this problem has recently been emphasized by studies presenting results from the *Spitzer Space Telescope* "From Molecular Cores to Planet Forming Disks" (cores to disks, hereafter c2d; Evans et al. 2003) Legacy Program. One of the first results to come from the c2d project was the discovery of very low luminosity objects (VeLLOs), objects embedded within dense cores with $L_{\rm int}$[4] $\leqslant 0.1\ L_{\odot}$, most in cores previously classified as starless (Young et al. 2004; Bourke et al. 2006; Dunham et al. 2006, 2008, 2010a; Di Francesco et al. 2007; Terebey et al. 2009; Lee et al. 2009). The discovery of such low luminosity protostars only exacerbated the existing luminosity problem. Furthermore, Dunham et al. (2008), Enoch et al. (2009b), and Evans et al. (2009) all examined protostellar luminosities from the c2d survey and showed that the protostellar luminosity distribution spans more than three orders of magnitude, is strongly skewed toward low luminosities (greater than 50% of protostars feature luminosities indicating $\dot{M} \lesssim 10^{-6}\ M_{\odot}\ {\rm yr}^{-1}$), and is inconsistent with the standard model as well as with the modifications described above, which tend to increase the mass accretion rate and thus make the problem worse.

One possible resolution to the luminosity problem is the idea that mass accretion is not constant. As noted by Kenyon et al. (1990), either accretion rates that decline with time or accretion rates that are very low most of the time but occasionally very high could resolve the luminosity problem. The latter process, commonly referred to as episodic accretion, features prolonged periods of lower-than-average accretion punctuated by short bursts of higher-than-average accretion, a scenario already invoked to explain the luminosity flares seen in FU Orionis objects

[4] The internal luminosity, $L_{\rm int}$, is the luminosity of the central source and excludes luminosity arising from external heating.

(Hartmann & Kenyon 1985). First proposed by Kenyon et al. (1990), such a solution was also suggested by Dunham et al. (2008), Enoch et al. (2009b), and Evans et al. (2009) as a plausible explanation for both the large spread in observed luminosities and the significant population of sources at low luminosities. Theoretical studies have provided several mechanisms for such a process in the embedded protostellar phase. Hydrodynamical and MHD simulations have demonstrated that material accreting from a core can pile up in a circumstellar disk until the disk becomes gravitationally unstable and fragments into spiral structure and dense clumps, which are then driven onto the protostar in short-lived accretion bursts generated through the gravitational torques associated with the spiral structure (Vorobyov & Basu 2005b, 2006, 2010; Machida et al. 2011). Numerical hydrodynamic simulations without self-consistent disk–core interaction but with gravitationally overstable massive disks have also shown quick migration of dense clumps into the disk inner region and probably onto the star (Boss 2002; Cha & Nayakshin 2011). Alternatively, several authors have explored a scenario where a similar process involving gravitational instabilities in the outer disk triggers rapid accretion into the inner disk; the subsequent heating of the inner disk by this accretion activates magnetorotational instabilities (MRI) that then drive material onto the protostar in short accretion bursts (Armitage et al. 2001; Zhu et al. 2009a, 2009b, 2010). Other possible mechanisms have been proposed as well, including quasi-periodic magnetically driven outflows in the envelope causing magnetically controlled accretion bursts (Tassis & Mouschovias 2005), decay and regrowth of MRI turbulence (Simon et al. 2011), close interaction in binary systems or in dense stellar clusters (Bonnell & Bastien 1992; Pfalzner et al. 2008), and disk–planet interaction (Lodato & Clarke 2004; Nayakshin & Lodato 2011).

Direct observational evidence for episodic mass accretion bursts in the embedded phase is less clear. Several Class I sources, including V1647 Ori (e.g., Ábrahám et al. 2004; Acosta-Pulido et al. 2007; Fedele et al. 2007; Aspin et al. 2009), OO Serpentis (Kóspál et al. 2007), [CTF93]216-2 (Caratti o Garatti et al. 2011), and VSX J205126.1 (Covey et al. 2011; Kóspál et al. 2011), have undergone recent flares attributed to accretion bursts. However, these sources only flared in $L_{\rm bol}$ by factors of ∼2–10, and all appear to be very late Class I sources near the end of the embedded phase with little remaining envelope material. On the other hand, the detection of silicate features and CO_2 ice bands in absorption in several known FU-Ori-like objects suggests the presence of massive envelopes (Quanz et al. 2007) and one of these objects, RHO 1B, has recently brightened by a factor of 1000 (Staude & Neckel 1991). Episodic mass ejection is seen in jets ejected from some protostellar systems, suggesting an underlying variability in the mass accretion, although the combination of jet velocities and spacing between knots often suggest shorter periods of episodicity than found by the above theoretical studies (e.g., Lee et al. 2007; Devine et al. 2009). Additionally, several Class 0 sources drive strong outflows implying higher average mass accretion rates than expected from their current luminosities (André et al. 1999; Dunham et al. 2006, 2010a; Lee et al. 2010) and Watson et al. (2007) showed a mismatch between the accretion rates onto the disk and protostar of NGC 1333-IRAS 4B, although their results are currently under debate (Herczeg et al. 2011). Finally, White & Hillenbrand (2004) showed that a sample of optically visible Class I sources in Taurus have very low accretion rates comparable to values observed for typical Class II sources rather than those expected for accreting Class I objects, although it is unclear if this result is simply a consequence of the Class I objects in their study being optically visible and thus very near the end of the embedded stage.

In this paper, we test the hypothesis that the accretion process predicted by Vorobyov & Basu (2005b, 2006, 2010), which includes both accretion rates that decline with time and episodic accretion bursts, can resolve the luminosity problem and match the observed properties of embedded protostars. We couple the hydrodynamic simulations presented by Vorobyov & Basu with radiative transfer models to calculate the observational signatures of cores collapsing to form protostars in the manner predicted by these simulations, and use these results to directly compare to observations. This work is a direct follow-up to two previous studies. In the first, Young & Evans (2005, hereafter Paper I) used a one-dimensional dust radiative transfer code to calculate the observational signatures of cores undergoing inside-out collapse following Shu (1977). They followed three different cores with initial masses of 0.3, 1, and 3 $M_\odot$ and showed that such models match only the upper end of the protostellar luminosity distribution, reconfirming the luminosity problem. In the second study, Dunham et al. (2010b, hereafter Paper II) revisited the models from Paper I with a two-dimensional radiative transfer code and showed that including improved dust opacities, a circumstellar disk and rotationally flattened envelope structure, mass loss, and outflow cavities improved the match to observations but did not fully resolve the luminosity problem, whereas a toy-model representation of episodic accretion could in fact resolve the luminosity problem. However, the latter conclusion is only tentative since the episodic accretion was included in a very simple manner where all mass accreted from the core builds up in the disk until the disk reaches 20% of the protostellar mass, at which point the accretion rate from the disk onto the star jumps from $0\,M_\odot$ yr^{-1} to $10^{-4}\,M_\odot$ yr^{-1} until the disk is fully drained of its mass. The accretion rate from the disk onto the star then drops back down to $0\,M_\odot$ yr^{-1} and the cycle begins anew. This simplification likely exaggerates the fraction of total mass accreted in bursts, as pointed out by Offner & McKee (2011; see also Section 5.4). Here we will revisit the Paper II results using accurate predictions for the evolution of collapsing cores from hydrodynamical simulations.

This paper is complementary to several other recent studies. Myers et al. (1998) presented simple radiative transfer calculations predicting observational signatures of collapsing cores, including an exponentially declining accretion rate with time and the effects of mass loss, and showed that such models could generally reproduce the median-observed protostellar luminosities but not the full range of values. However, their model evolution is not based on a fully self-consistent analytic or numerical model. Lee (2007) modified the Paper I model to include episodic accretion in a very simple manner in order to study the effects such a process has on the chemical evolution of collapsing cores. Vorobyov (2009b) compared the distribution of mass accretion rates in their simulations featuring episodic accretion (Vorobyov & Basu 2005b, 2006) to those inferred from the luminosities of protostars in the Perseus, Serpens, and Ophiuchus molecular clouds compiled by Enoch et al. (2009b) and showed that their simulations reproduced some of the basic features of the observed distribution of mass accretion rates. However, the observed distribution of accretion rates is quite uncertain since it is calculated from the observed protostellar luminosity distribution with assumed values for the protostellar masses and radii and with the assumption that all observed luminosity is

accretion luminosity. Finally, Offner & McKee (2011) presented analytic derivations of the protostellar luminosity distribution for different models and concluded that models that tend toward a constant accretion time rather than constant accretion rate produce a greater spread in luminosities and are in better agreement with observations, similar to the result obtained by Myers (2010) that analytic models with accretion rates that increase with mass can at least partially resolve the luminosity problem. However, both Offner & McKee (2011) and Myers (2010) simply compared theoretical luminosities with the observed protostellar luminosity distribution, whereas this study uses radiative transfer calculations to "observe" the underlying theory (in this case, the Vorobyov & Basu simulations) in a manner consistent with, and with direct comparison to, the observations.

The organization of this paper is as follows. A brief description of the models is provided in Section 2, focusing on the hydrodynamical simulations in Section 2.1 and the radiative transfer models in Sections 2.2. 3 describes how the models are turned into observational signatures and the observational data set to which the models are compared, while Section 4 describes the basic results. A discussion of these results is presented in Section 5, focusing on the degree to which the models resolve the luminosity problem in Section 5.1, the match between observed and model bolometric temperatures in Section 5.2, the duration of the embedded phase in Section 5.3, and the number, duration, and importance of the mass accretion bursts in Section 5.4. Finally, a basic summary of our results and conclusions is given in Section 6.

2. DESCRIPTION OF THE MODEL

In this section, we provide a description of both the hydrodynamical simulations of collapsing cores used to predict the time evolution of physical quantities such as masses, radii, and accretion rates (Section 2.1), and the radiative transfer models used to calculate the observational signatures of collapsing cores following these simulations (Section 2.2). The radiative transfer models are based on those previously presented in Papers I and II, thus we only summarize the most important information and refer the reader to Papers I and II for significantly more detailed descriptions of these models. Additionally, we note here that the terms "core" and "envelope" are sometimes used interchangeably in the literature, whereas other times they are used separately to distinguish between circumstellar material of different densities, different states (bound versus unbound), etc. In this paper, we exclusively use the term core to refer to the full population of dense material which collapses to form a star, and do not use the term envelope at all. In our usage the term core is interchangeable with what is commonly referred to as the envelope in continuum radiative transfer studies, including in Papers I and II.

2.1. Hydrodynamical Simulations

2.1.1. Basic Processes and Equations

We make use of numerical hydrodynamics simulations in the thin-disk approximation to compute the gravitational collapse of rotating, gravitationally bound, pre-stellar cores. This approximation is an excellent means to calculate the evolution for many orbital periods and many model realizations. It is valid as long as the aspect ratio A of the disk scale height h to radius r is well below unity, which is usually fulfilled in the inner 1000 AU (see Figure 11 in Vorobyov & Basu 2010). Protostellar disks rarely exceed 1000 AU in radius (Vicente & Alves 2005; Vorobyov 2011), making our approach well justified for the purpose of collecting a wide statistical sample of model disks. At larger radial distances, A may approach unity but those regions are not important dynamically and serve as a reservoir for material falling onto the disk during the embedded phase of star formation.

We start our numerical integration in the pre-stellar phase characterized by a collapsing *starless* core, continue into the embedded phase of star formation during which a star and disk are formed, and terminate our simulations in the T Tauri phase when most of the core has accreted onto the forming star+disk system. The thin-disk approximation allows us to consider spatial scales of order 10,000 AU and compute the evolution of both the core and the star+disk system altogether. An important consequence is that the mass accretion rate onto the disk ($\dot{M}_d$) is not a free parameter of our model but is self-consistently determined by the gas dynamics in the collapsing core.

We introduce a "sink cell" at $R_{\rm sc} = 6$ AU and allow for the matter in the computational domain to freely flow into the sink cell but not out of it. We monitor the gas density in the sink cell and when its value exceeds a critical value for the transition from isothermal to adiabatic evolution ($\sim 10^{11}$ cm^{-3}), we introduce a central gravitating point-mass star. In the subsequent evolution, most of the gas that crosses the inner boundary is assumed to land onto the central star while a small fraction is assumed to be carried away with protostellar jets, with the exact partition being a free parameter (usually 10% is assumed to be ejected).

The main physical processes that are taken into account in our modeling include stellar irradiation, background irradiation with temperature $T_{\rm bg} = 10$ K, viscous and shock heating, radiative cooling from the disk surface, and also disk self-gravity. The corresponding equations of mass, momentum, and energy transport are

$$\frac{\partial \Sigma}{\partial t} = -\nabla_p \cdot (\Sigma \boldsymbol{v}_p), \tag{1}$$

$$\frac{\partial}{\partial t}(\Sigma \boldsymbol{v}_p) + [\nabla \cdot (\Sigma \boldsymbol{v}_p \otimes \boldsymbol{v}_p)]_p = -\nabla_p \mathcal{P} + \Sigma \boldsymbol{g}_p + (\nabla \cdot \boldsymbol{\Pi})_p, \tag{2}$$

$$\frac{\partial e}{\partial t} + \nabla_p \cdot (e \boldsymbol{v}_p) = -\mathcal{P}(\nabla_p \cdot \boldsymbol{v}_p) - \Lambda + \Gamma + (\nabla \boldsymbol{v})_{pp'} : \Pi_{pp'}, \tag{3}$$

where subscripts p and p' refer to the planar components (r, ϕ) in polar coordinates, Σ is the mass surface density, e is the internal energy per surface area, $\mathcal{P} = \int_{-h}^{h} P dh$ is the vertically integrated form of the gas pressure P, h is the radially and azimuthally varying vertical scale height determined in each computational cell using an assumption of local hydrostatic equilibrium, $\boldsymbol{v}_p = v_r \hat{\boldsymbol{r}} + v_\phi \hat{\boldsymbol{\phi}}$ is the velocity in the disk plane, $\boldsymbol{g}_p = g_r \hat{\boldsymbol{r}} + g_\phi \hat{\boldsymbol{\phi}}$ is the gravitational acceleration in the disk plane, and $\nabla_p = \hat{\boldsymbol{r}} \partial/\partial r + \hat{\boldsymbol{\phi}} r^{-1} \partial/\partial \phi$ is the gradient along the planar coordinates of the disk. Viscosity enters the basic equations via the viscous stress tensor $\boldsymbol{\Pi}$ and the magnitude of kinematic viscosity ν is parameterized using the usual α-prescription of Shakura & Sunyaev (1973). In our models, we use a spatially and temporally uniform α, with its value set to 5×10^{-3}.

Apart from viscous heating determined by the viscous stress tensor $\boldsymbol{\Pi}$, the thermal balance of the disk is also controlled by heating due to stellar and background irradiation and radiative cooling from the disk surface. The latter is calculated using

the diffusion approximation of the vertical radiation transport in a one-zone model of the vertical disk structure (Johnson & Gammie 2003):

$$\Lambda = \mathcal{F}_c \sigma\, T^4 \frac{\tau}{1+\tau^2}, \quad (4)$$

where σ is the Stefan–Boltzmann constant, T is the midplane temperature of gas, and $\mathcal{F}_c = 2 + 20\tan^{-1}(\tau)/(3\pi)$ is a function that secures a correct transition between the optically thick and thin regimes. We use frequency-integrated opacities τ of Bell & Lin (1994).

The heating function is expressed as

$$\Gamma = \mathcal{F}_c \sigma\, T_{\rm irr}^4 \frac{\tau}{1+\tau^2}, \quad (5)$$

where $T_{\rm irr}$ is the irradiation temperature at the disk surface determined by the stellar and background blackbody irradiation as

$$T_{\rm irr}^4 = T_{\rm bg}^4 + \frac{F_{\rm irr}(r)}{\sigma}, \quad (6)$$

where $T_{\rm bg}$ is the uniform background temperature (in our model set to the initial temperature of the natal cloud core) and $F_{\rm irr}(r)$ is the radiation flux (energy per unit time per unit surface area) absorbed by the disk surface at radial distance r from the central star. The latter quantity is calculated as

$$F_{\rm irr}(r) = \frac{L_*}{4\pi r^2}\cos\gamma_{\rm irr}, \quad (7)$$

where the incidence angle of radiation $\gamma_{\rm irr}$ arriving at the disk surface at radial distance r is calculated using the model's known radial profile of the disk scale height h, and L_* is the sum of the accretion luminosity $L_{*,\rm accr}$ arising from the gravitational energy of accreted gas and the photospheric luminosity $L_{*,\rm ph}$ due to gravitational compression and deuterium burning in the star interior. While the former quantity is calculated from the model's known stellar mass and accretion rate onto the star, the latter is taken from the pre-main-sequence tracks of D'Antona & Mazzitelli (1994). A more detailed explanation of the model can be found in Vorobyov & Basu (2010).

2.1.2. Initial Conditions

The form of the initial gas density, temperature and angular velocity profiles in gravitationally bound, dense pre-stellar cores may vary depending on the environment and physical processes that contribute to the formation of such cores. In this work, we consider two possible gas surface density Σ and angular velocity Ω profiles and assume that the initial gas temperature in the core is equal to $T_{\rm init} \equiv T_{\rm bg} = 10$ K. Most models' cores have Σ and Ω typical for magnetically supercritical cores formed by slow gravitational contraction (Basu 1997):

$$\Sigma = \frac{r_0\Sigma_0}{\sqrt{r^2 + r_0^2}}, \quad (8)$$

$$\Omega = 2\Omega_0 \left(\frac{r_0}{r}\right)^2 \left[\sqrt{1+\left(\frac{r}{r_0}\right)^2} - 1\right], \quad (9)$$

where Ω_0 is the central angular velocity and r_0 is the radius of central near-constant-density plateau defined as $r_0 = \sqrt{A}c_s^2/(\pi G\Sigma_0)$, where c_s is the sound speed. These initial profiles are characterized by the important dimensionless free parameter $(\Omega_0 r_0/c_s)^2$ and have the property that the ratio of rotational to gravitational energy $\beta \approx 0.91(\Omega_0 r_0/c_s)^2$ (see Basu 1997). We note that the above form of the column density is very similar to the integrated column density of a Bonnor–Ebert sphere with a positive density enhancement A (Dapp & Basu 2009). Throughout the paper, we use $A = 1.2$. In addition, every core is truncated so that the ratio of the core radius to the radius of the central flat region $r_{\rm core}/r_0$ is constant and equal to 6.0. The truncation mechanisms could be erosion of the core outer regions by UV radiation and/or tidal stripping.

The actual procedure for generating a specific core is as follows. First, we fix β between approximately 10^{-3} and 10^{-2} based on observational results that find that β ranges between approximately 10^{-4} and 10^{-1} (Goodman et al. 1993; Caselli et al. 2002).[5] Then we fix the core radius $r_{\rm core}$ and find r_0 from the condition $r_{\rm core}/r_0 = 6$. The central surface density Σ_0 is found from the relation $r_0 = \sqrt{A}c_s^2/(\pi G\Sigma_0)$ and the resulting core mass $M_{\rm core}$ is determined from Equation (8). Finally, the central angular velocity Ω_0 is found from the condition $\beta = 0.9(\Omega_0 r_0/c_s)^2$.

As an alternative to the $\Sigma \propto r^{-1}$ and $\Omega \propto r^{-1}$ profiles, we also consider several models with radially constant Σ and Ω distributions, corresponding to self-gravitating, sheet-like cores with volume density depending only on distance from the midplane $\rho(z) = \rho(0)\,\mathrm{sech}^2(z/h)$ (Boss & Hartmann 2001).

In total, we have considered 23 models with initial core masses ($M_{\rm core}$) ranging from 0.105 $M_\odot$ to 1.84 $M_\odot$ and initial ratios of rotational to gravitational energy $\beta = (0.275\text{–}1.26) \times 10^{-2}$. The parameters of these 23 models are summarized in Table 1. The left panel of Figure 1 plots the mass-weighted initial angular velocity versus initial core mass for each model, where we have chosen to plot the mass-weighted rather than central angular velocity for direct comparison to observations. Our models range from about 10^{-14} rad s^{-1} to a few times 10^{-13} rad s^{-1}, consistent with the observed range found by Goodman et al. (1993). The right panel of Figure 1 plots the distribution of initial core masses for each model. The absence of models with $M_{\rm core} > 2.0\,M_\odot$ is caused by numerical difficulties associated with modeling the collapse of massive cores. We plan to extend our parameter space in a future study. This distribution clearly does not follow the stellar initial mass function (IMF). However, all results in this paper are presented after weighting each individual model by the IMF in order to properly compare to observations (see Section 4 for details on this weighting). Our results are thus robust to the exact number of models at different masses as long as we adequately sample all relevant mass ranges.

Figure 2 plots the time evolution of the accretion rate onto the protostar ($\dot{M}_s$) for each of the 23 models considered in this paper and listed in Table 1. The accretion is highly variable with episodic bursts of rapid accretion, with the exact amplitude and frequency of the variability differing from one model to the next due to the different initial conditions (in particular initial core mass; see Vorobyov & Basu 2010 for details). The origin of the accretion variability seen in Figure 2 is discussed in detail below in Section 2.1.3. One particular feature worth noting in Figure 2 is that the average accretion rates show a gradual decline with time. On timescales of ~ 1.0 Myr the decline in $\dot{M}$ may reach three orders of magnitude. This behavior is likely caused by a

[5] While both Goodman et al. (1993) and Caselli et al. (2002) find that approximately 50% of observed cores have β between 10^{-2}and10^{-1}, we are unable to consider models with $\beta \gtrsim 10^{-2}$ due to technical limitations and thus may be biased against cores with high initial rotation and angular momentum.

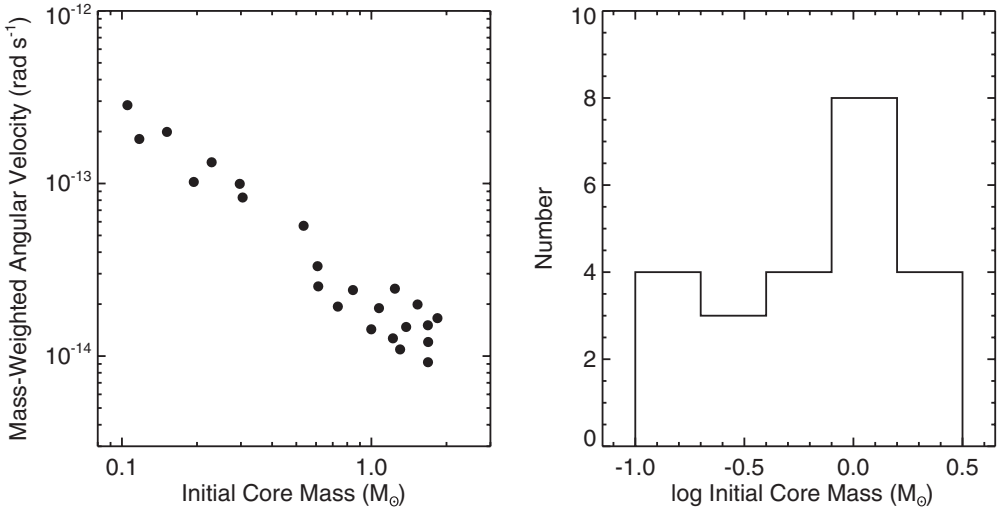

Figure 1. Left: mass-weighted initial angular velocity for the 23 models considered in this paper and listed in Table 1. Right: histogram showing the distribution of initial core masses in log space with bins 0.3 dex wide.

Table 1
Model Parameters

Model	Ω_0 (rad s^{-1})	r_0 (AU)	Σ_0 (g cm^{-2})	Core Outer Radius (pc)	Initial Core Mass ($M_\odot$)	β
1	1.6×10^{-13}	685	0.18	0.02	0.305	8.75×10^{-3}
2	1.95×10^{-13}	685	0.18	0.02	0.305	1.26×10^{-2}
3	3.0×10^{-14}	3770	0.033	0.11	1.684	8.8×10^{-3}
4[a]	2.5×10^{-14}	...	0.026	0.04	0.612	8.75×10^{-3}
5[a]	0.9×10^{-14}	...	9.3×10^{-3}	0.11	1.686	8.8×10^{-3}
6[a]	1.2×10^{-14}	...	0.013	0.08	1.22	8.8×10^{-3}
7	2.0×10^{-13}	445	0.28	0.013	0.194	5.6×10^{-3}
8	2.3×10^{-14}	3770	0.033	0.11	1.689	5.6×10^{-3}
9	2.6×10^{-13}	514	0.24	0.015	0.229	1.26×10^{-2}
10	2.9×10^{-14}	3085	0.04	0.09	1.378	5.6×10^{-3}
11	3.2×10^{-14}	4115	0.03	0.12	1.84	1.26×10^{-2}
12	3.7×10^{-14}	2400	0.05	0.07	1.0726	5.6×10^{-3}
13	3.8×10^{-14}	1645	0.075	0.048	0.7337	2.75×10^{-3}
14	3.9×10^{-13}	342	0.36	0.01	0.1515	1.26×10^{-2}
15	3.9×10^{-14}	3430	0.036	0.1	1.5312	1.26×10^{-2}
16	3.25×10^{-13}	274	0.45	0.008	0.1174	5.6×10^{-3}
17	4.7×10^{-14}	1885	0.066	0.055	0.8434	5.6×10^{-3}
18	4.8×10^{-14}	2745	0.045	0.08	1.2422	1.26×10^{-2}
19	5.56×10^{-13}	240	0.52	0.007	0.1052	1.26×10^{-2}
20	1.1×10^{-13}	1200	0.1	0.035	0.5349	1.26×10^{-2}
21	6.0×10^{-14}	1370	0.09	0.04	0.6084	5.6×10^{-3}
22	2.8×10^{-14}	2230	0.056	0.065	0.999	2.75×10^{-3}
23	2.0×10^{-14}	2915	0.043	0.085	1.304	2.75×10^{-3}

Note. [a] Constant surface density profile model.

gradual decline of the disk mass with time, which is particularly prominent starting from the late Class I phase when mass loading from the parent core diminishes (Vorobyov 2009a, 2011).

2.1.3. Disk Gravitational Instability and Variable Accretion

As was discussed in Section 1, episodic accretion is a plausible solution to the luminosity problem and various physical processes have been invoked to produce episodic and repetitive bursts of mass accretion onto the star. Among them, disk gravitational instability and fragmentation in the embedded phase of star formation has been shown to trigger intense bursts of accretion luminosity as the forming fragments are torqued into the disk inner regions and onto the star (Vorobyov & Basu 2005b, 2006, 2010; Machida et al. 2011). Apart from these FU-Ori-like bursts, gravitationally unstable disks are generally characterized by highly variable accretion onto the star caused by the nonlinear interaction of dominant spiral modes (Vorobyov 2009b) or by the presence of a massive planet (Machida et al. 2011). In this section, we take model 12 as a prototype model and use this model to illustrate the role of disk gravitational instability and fragmentation in driving variable accretion onto the star.

First, we must discuss the method by which we calculate basic disk properties. The disk mass and radius are calculated at each time step by disentangling the disk and infalling core on the computational mesh. We do this in practice by adopting

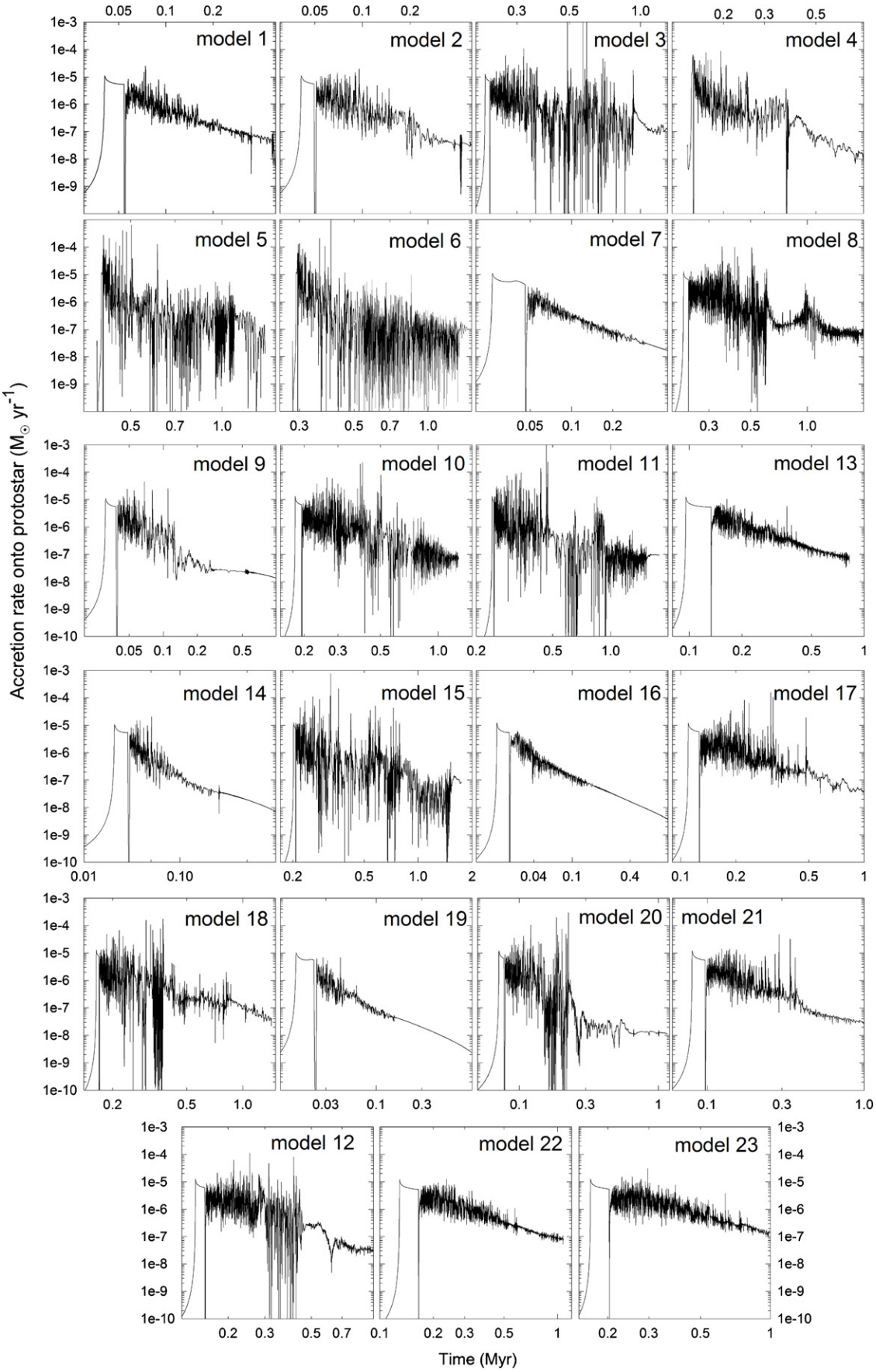

Figure 2. Time evolution of the mass accretion rate onto the protostar for each of the 23 models considered in this paper and listed in Table 1. The zero time is defined from the beginning of the collapse of pre-stellar cores. Note that the full duration of each model is shown here, whereas the embedded phase is considered to end when 10% of the initial core mass remains (see Section 2.2). Note that the scale of the *x*-axis varies from one panel to the next depending on the total duration of each model.

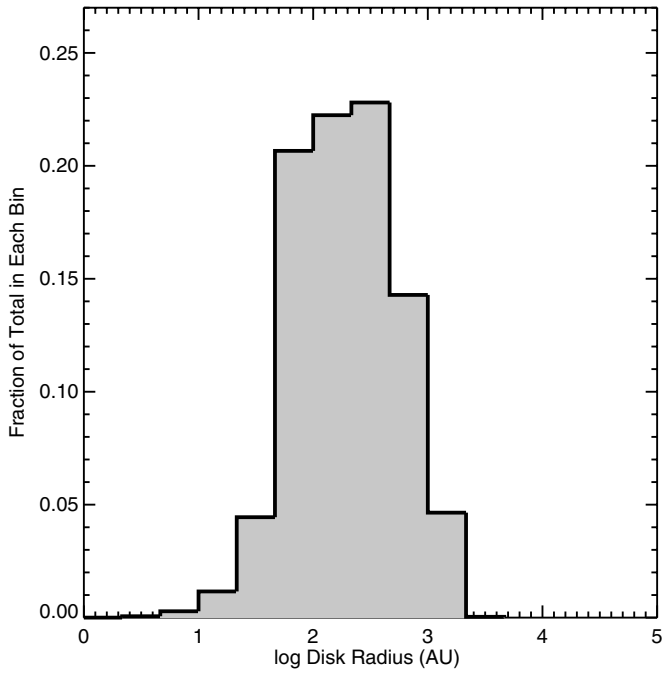

Figure 3. Histogram showing the fraction of total time spent by all models at various $R_{\rm disk}$, weighted by the initial mass function as described in Section 4. The bin size is 1/3 dex.

a surface density threshold of 0.5 g cm^{-2} between the disk and core and also using the radial gas velocity profile. This method is described in detail by Vorobyov (2011), although we note that Vorobyov (2011) adopted a lower surface density threshold of 0.1 g cm^{-2}. The values of the disk radius and mass both depend on the adopted threshold. Figure 3 plots a histogram showing the fraction of total time the 23 models considered in this paper spend at various disk radii (weighted by the IMF; see Section 4). Our choice of a threshold of 0.5 g cm^{-2} is motivated by the fact that the resulting distribution of disk radii peaks between 10^2 and 10^3 AU; adopting the original 0.1 g cm^{-2} threshold would shift the entire distribution up by about a factor of 2–3. Sizes of *embedded* disks are very poorly constrained by observations and are typically assumed to be on the order of 100 AU or less based on simple centrifugal radius arguments. In reality, however, angular momentum transport will cause disks to spread to sizes greater than the centrifugal radii. Furthermore, there are some limited observations supporting the existence of large protostellar disks (i.e., the 1 $M_\odot$, 300 AU disk surrounding Serpens FIRS 1; Enoch et al. 2009a). Ultimately, the correct threshold to adopt in order to disentangle the disk and core in the simulations will remain uncertain until the masses and sizes of protostellar disks are better constrained.

Figure 4 presents gas surface density maps for model 12 at several times after the formation of the central star. Only the inner 1200 AU are shown, while the whole computational region amounts to 28,000 AU. The evolutionary times are chosen so as to emphasize three distinct stages of the disk evolution, each depicted by a separate row of images. The upper row shows the initial stage of the disk formation and growth. The disk begins to form at $t \approx 0.015$ Myr and several distinct fragments are present as early as at $t = 0.1$ Myr. The number of fragments varies with time due to the continuing process of disk fragmentation and migration of the fragments onto the star. At around $t = 0.16$ Myr the second stage of the disk evolution begins when a massive fragment ($\approx$0.15 $M_\odot$) forms in the disk. The fragment is prominent until $t = 0.3$ Myr when it is ejected from the disk via many-body interaction with other newly born fragments. This ejection event is very transient and is not captured in Figure 4 but is evident in Figure 5 showing the time evolution of the total mass in our computational domain. This is a universal mechanism that seems to occur in massive disks and is reported in other numerical studies of disk fragmentation (Stamatellos & Whitworth 2009; Bate 2009; Basu & Vorobyov 2011). After the ejection event, the last stage of disk evolution ensues, which is shown in the bottom row of Figure 4 and is characterized by a dramatic change in the disk appearance—the disk is no longer prone to fragmentation and shows only a weak spiral structure that diminishes with time. We note that these three stages are only indicative and reflect the overall tendency of a protostellar disk to go through the initially vigorously unstable phase toward a marginally stable configuration. All three stages are often observed in relatively massive disks. In low-mass disks, the first and second stages may be very short or even absent and the ejection event may not be present even in massive enough disks (Basu & Vorobyov 2011).

The three stages of the disk evolution are reflected in the mass accretion rate onto the star, $\dot{M}_{\rm s} = -2\pi R_{\rm sc} v_r \Sigma$, which we calculate as the mass passing through the sink cell per one time step of numerical integration (which in physical units is usually equal to 10–20 days and the total integration time can go beyond 1 Myr). The latter value is also corrected for the jet efficiency to account for the mass that passes through the sink cell but is later evacuated with the jets. We note that the adopted size of the sink cell $R_{\rm sc} = 6$ AU is larger than the stellar radius, except for the very early stage when the forming star is represented by the first hydrostatic core (FHSC). Decreasing $R_{\rm sc}$ entails a significant increase in the calculation times because the physical size of the computational zones in the ϕ-direction decreases as one approaches the singularity at $r = 0$, causing a corresponding decrease in the time step. Simultaneously, the number of grid zones in the r-direction needs to be increased to sustain an adequate resolution at $r \sim 100$ AU on the log-spaced grid. This effectively limits our choice of $R_{\rm sc}$ to a few AU at best considering the available computational resources. We acknowledge that our results may be sensitive to this limitation. For instance, additional accretion bursts may be triggered in the inner disk at $r < 6$ AU due to the thermal ionization instability (Bell & Lin 1994), MRI (Zhu et al. 2009a, 2009b), or disk–planet interaction (Nayakshin & Lodato 2011). We have run a few models with $R_{\rm sc} = 2$ AU and found that the general behavior of the accretion rates (variability, burst magnitudes) remains qualitatively similar but further work is needed to extend the computational region still closer to the stellar surface.

The time evolution of the mass accretion rate is shown in Figure 6. $\dot{M}_s$ is negligible in the pre-stellar phase and rises to a maximum value of 1.3×10^{-5} $M_\odot$ yr^{-1} when the FHSC forms at $t = 0$ Myr (the time is counted from this moment). The subsequent short period of evolution is characterized by a gradually declining $\dot{M}_s$ when the material from the core lands directly onto the forming star. A sharp drop in the accretion rate at $t = 0.015$ Myr manifests the beginning of the disk formation phase when the infalling core material hits the centrifugal barrier near the sink cell and the accretion rates drops to zero. However, the process of mass loading from the core continues, the disk grows in mass and size, and gravitational instability is soon ignited in the disk at $t = 0.04$ Myr. From this moment and until $t = 0.16$ Myr, i.e., during the first stage of disk

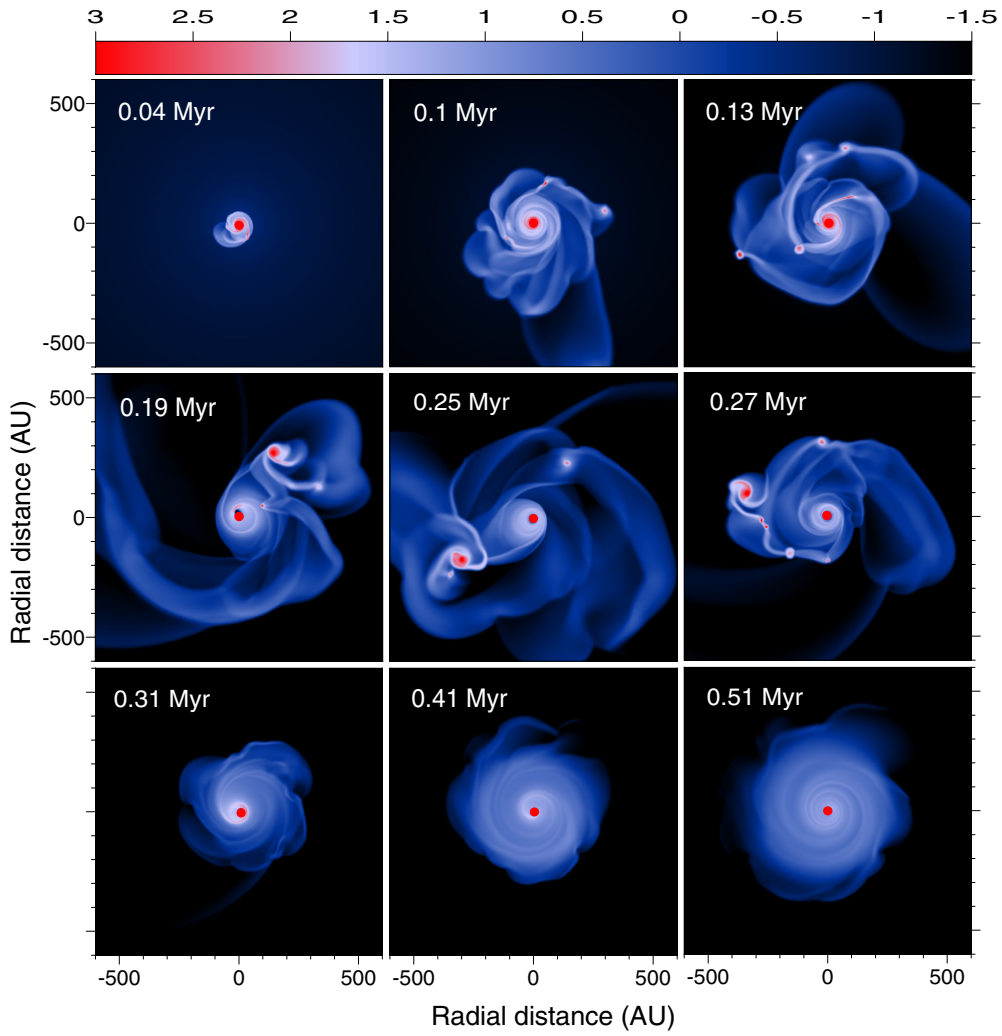

Figure 4. Model 12 gas surface densities in the inner 1200 AU at several times after the formation of the central. The star is shown in the coordinate center by a red circle and the time is shown in each panel in Myr. The scale bar is in g cm^{-2}. Vigorous gravitational instability and fragmentation is evident in the early disk evolution at 0.1 Myr $\lesssim t \lesssim$ 0.3 Myr.

(A color version of this figure is available in the online journal.)

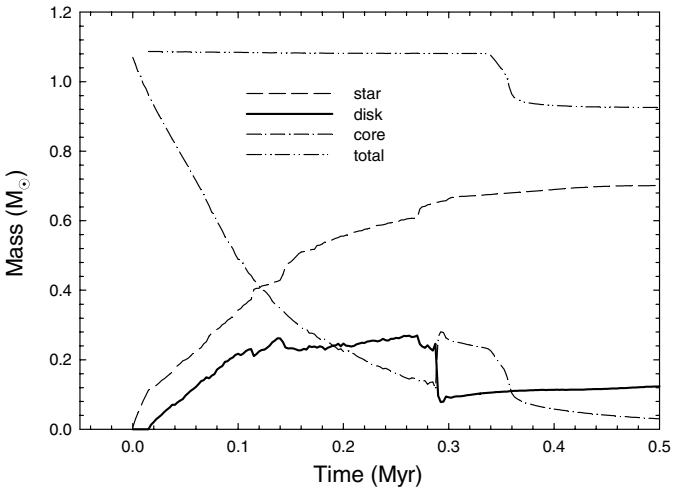

Figure 5. Time evolution of the disk, stellar, and core masses, as well as the total mass in the computational domain, for model 12. The zero time is defined as the moment of formation of the central star.

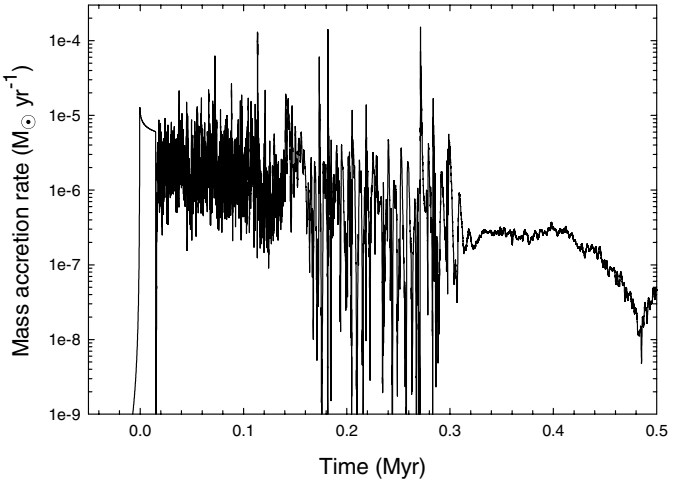

Figure 6. Time evolution of the mass accretion rate onto the star for model 12. The zero time is defined as the moment of formation of the central star.

evolution, accretion exhibits variability with periods in the 400–1000 yr range and rates between a few $\times 10^{-7}\,M_\odot$ yr^{-1} and a few $\times 10^{-5}\,M_\odot$ yr^{-1} and also several strong bursts with $\dot{M}_s \gtrsim 2 \times 10^{-5}\,M_\odot$ yr^{-1}. The latter are caused by fragments migrating onto the star due to the loss of angular momentum via gravitational interaction with spiral arms in the disk (Vorobyov & Basu 2005b, 2006, 2010). The typical period of accretion variability implies that its driving force lies in the disk intermediate regions at $r = 30$–60 AU (for an average stellar mass $0.3\,M_\odot$). Many theoretical and numerical studies, including our own, indicate that this is the minimum distance from the star at which gravitational instability and fragmentation can occur (e.g., Stamatellos & Whitworth 2008; Clarke 2009; Vorobyov & Basu 2010; Meru & Bate 2010), suggesting a causal link between the disk gravitational instability and accretion variability in our model.

During $t = 0.16$–0.3 Myr, i.e., during the second stage of disk evolution, the accretion pattern changes notably and starts to show a higher-amplitude and longer-period variability, with accretion rates lying between $10^{-10}\,M_\odot$ yr^{-1} and a few $\times 10^{-4}\,M_\odot$ yr^{-1}. This change is caused by the formation of a massive fragment clearly visible in the middle row in Figure 4. The typical period of accretion variability is now $\approx 5 \times 10^3$ yr, implying that the driving force is located at $r \approx 250$ AU. This value is an average orbital distance of the fragment, suggesting a causal link between accretion variations and orbital motion of the fragment. A similar correlation between the orbital period of a massive object in the disk and the accretion rate variability was found by Machida et al. (2011). These results demonstrate that the disk gravitational instability and fragmentation are the driving forces for the accretion variability in our models.

During $t = 0.3$–0.5 Myr, i.e., during the third stage of disk evolution, accretion onto the star again undergoes a dramatic change. There are no more bursts or high-amplitude variations. $\dot{M}_s$ shows a gradual decline with time from a few $\times 10^{-7}\,M_\odot$ yr^{-1} to a few $\times 10^{-8}\,M_\odot$ yr^{-1} with only low-amplitude flickering. This change is caused by the ejection of the massive fragment from the disk and the associated loss of a significant fraction of the disk material. As a result, the disk settles into a state with only marginal gravitational instability characterized by a weak and diffuse spiral structure. At this stage, the accretion rate is mostly determined by viscous torques rather than by gravitational ones (Vorobyov & Basu 2009a).

We caution that accretion rates may be sensitive to our choice of the α-parameter, which determines the magnitude of viscous torques in our model. In the present study, we use a spatially and temporally uniform $\alpha = 5 \times 10^{-3}$, a value chosen for consistency with the work of Vorobyov & Basu (2009b, 2010). These authors studied numerically the secular evolution of viscous and self-gravitating disks, with particular emphasis on accretion rates, and found that $\alpha < 10^{-2}$ is needed to reproduce both the FU Ori accretion bursts and the range and magnitude of accretion rates found for brown dwarfs and T Tauri stars.

However, the α-parameter may vary in space and time. In particular, if the gas surface density exceeds some critical value (a few $\times$ 100 g cm^{-2}; Armitage 2011), then the ionization fraction due to cosmic rays and X-rays becomes insufficient to sustain the MRI and the corresponding α-parameter is expected to decrease significantly. In this case, the outburst phenomenon, in particular, and the accretion variability, in general, will be more pronounced as demonstrated by Vorobyov & Basu (2009a, 2010). In our models, surface densities in excess of the critical value are found in the inner 10–20 AU for relatively massive

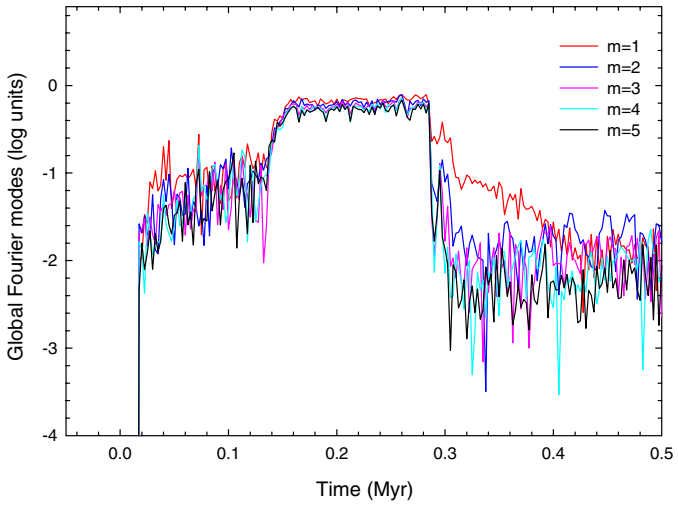

Figure 7. Time evolution of the first five global Fourier amplitudes for model 12. The amplitudes are plotted in log units. The zero time is defined as the moment of formation of the central star.

(A color version of this figure is available in the online journal.)

disks (Vorobyov 2010). This means that our choice of a fixed $\alpha = 5 \times 10^{-3}$ may cause the outburst magnitude to damp somewhat in the inner parts of the disk.

Figure 7, which plots the time evolution of the global Fourier modes, substantiates our analysis. We calculate the first five modes using the following equation:

$$C_{\rm m}(t) = \frac{1}{M_{\rm disk}} \left| \int_0^{2\pi} \int_{R_{\rm sc}}^{R_{\rm disc}} \Sigma(r, \phi, t)\, e^{im\phi} r\, dr\, d\phi \right|, \qquad (10)$$

where $M_{\rm disk}$ is the disk mass and $R_{\rm disk}$ is the disk's physical outer radius.

Three distinct patterns of modal behavior are seen in Figure 7, each corresponding to a particular stage of disk evolution. In the early evolution at $t = 0.04$–0.16 Myr, the nonlinear interaction between competing spiral modes in the gravitationally unstable disk gives rise to the mode variability resembling in magnitude and frequency that of the mass accretion rate.[6] At $t = 0.16$–0.3 Myr, global modes are maximal (with lower order modes being marginally dominant) but show little variability, while the corresponding accretion rates are highly variable. The matter that is the dominant source of perturbation is now a massive compact fragment, and the accretion variability is driven by the dynamics of the fragment rather than by the nonlinear interaction of the spiral modes. After $t = 0.3$ Myr, the global modes show a fast decline by two orders of magnitude caused by a sharp decrease in the disk mass after the ejection event. Although the modes return to a highly variable pattern, their amplitudes are very low, $\sim 10^{-2}$, meaning that the non-axisymmetric density perturbations in the disk at this stage are of the order of 1% and the mass accretion is now entirely controlled by viscous torques. The latter drive the disk toward an axisymmetric state (Vorobyov & Basu 2009a) and the corresponding accretion rates show only low-amplitude flickering, gradually declining as the disk is drained of its mass reservoir.

The time evolution of the disk, core, and stellar mass as well as the total star+disk+core mass in the computational domain

[6] The output frequency with which the modes are calculated is lower than that of the mass accretion rate. This should be taken into account when comparing Figures 6 and 7.

were shown in Figure 5. It is worth noting that the stellar mass is always greater than that of the disk. This is a direct consequence of the regulating nature of the accretion burst phenomenon. The interplay between mass loading from the core and migration of the fragments onto the star helps to sustain the system near the fragmentation boundary, with the disk periodically going above and below this boundary until the infalling core is depleted of matter (Vorobyov & Basu 2006, 2010). The ejection event is well visible in the time evolution of the disk, core, and total mass. Both the disk and core exhibit a sharp change in mass at $t \approx 0.3$ Myr, with the disk losing mass and the core gaining mass as the fragment leaves the disk and propagates radially outward through the core. At $t \approx 0.34$ Myr, the fragment passes through the outer computational boundary at $r = 14{,}000$ AU, which is manifested by a sharp drop in the total mass in the computational domain. From the amplitude of this drop, we can estimate the upper limit on the mass of the fragment as $0.15\ M_{\odot}$. This estimate includes the fragment itself as well as a mini-disk that surrounds it.

2.2. Radiative Transfer Models

An ideal coupling of hydrodynamic simulations with radiative transfer models involves taking the detailed disk and core structure from the former and using them as inputs to the latter. Our hydro simulations, however, provide the radial structure and the disk vertical scale height but lack the detailed vertical density and temperature distributions (due to the adopted thin-disk approximation) needed to run radiative transfer models. One way to circumvent this difficulty would be to reconstruct the disk and core vertical structure solving for the combined equations of vertical hydrostatic equilibrium and vertical radiation transfer after updating the flow variables in the plane of the disk. This approach, which would render our hydro simulations essentially two plus one dimensional, is currently under development and will be presented in a future paper.

In this work, we have employed a simpler approach by taking analytic profiles for the core and disk structure and re-scaling them according to simulation's known parameters. More specifically, for each of the models listed in Table 1, the hydro simulations described above provide the initial core mass ($M_{\rm core}$) and radius[7] ($r_{\rm core}$), along with the time evolution of the core mass, disk mass ($M_{\rm disk}$), protostellar mass ($M_{\rm star}$), disk outer radius ($R_{\rm disk}$), accretion rate onto the protostar ($\dot{M}_s$), and accretion rate onto the disk ($\dot{M}_d$). These parameters are used to construct the core and disk structure according to analytic profiles described in more detail below. Incorporating the exact physical structure at each time step from the simulations will not fundamentally alter our results or conclusions since the mass and radius of the protostar and disk and accretion rates onto both objects are unchanged, but it will affect the detailed comparison to observations since the radiative transfer (and thus resulting core temperature profile, spectral energy distributions (SEDs), and observational signatures) depends on the two-dimensional physical structure.

As in Papers I and II, the core inner radius is held fixed at a value such that the initial optical depth at 100 μm is set equal to 10 (see Paper I, in particular Equation (4)) until the disk outer radius exceeds this value; once this occurs the core inner radius is set equal to the disk outer radius. Following both Papers I and II and Vorobyov & Basu (2010), the protostellar radius ($R_{\rm star}$) is calculated from $M_{\rm star}$ following Palla & Stahler (1991; see Equation (11) of Vorobyov & Basu 2010), except at early times where it is modified to take into account the FHSC (Larson 1969) stage. Following Vorobyov & Basu, $R_{\rm star}$ is fixed at 5 AU for the duration of the FHSC phase and then smoothly joined to the Palla & Stahler values over a period of 1000 yr when the second core forms. We use a simple polytropic model for the forming star and assume that the transition from the FHSC to the second core (protostar) occurs when the central temperature exceeds 2×10^3 K. This is an improved implementation of $R_{\rm star}$ as compared to that in Papers I and II but it yields similar lifetimes of the FHSC, (1–2) $\times 10^4$ yr.

As in Paper II, we adopt the core density profile given by the TSC84 solution for the collapse of a slowly rotating core to include the effects of rotational flattening. The TSC84 solution results in a core that is initially a spherically symmetric, singular isothermal sphere with a density distribution $n \propto r_{\rm core}^{-2}$, identical to the Shu (1977) solution. As collapse proceeds, the solution takes on two forms: an outer solution that is similar to the non-rotating, spherically symmetric solution and an inner solution that exhibits flattening of the density profile. Since material falling into the central regions originates from larger radii and thus carries more angular momentum as time progresses, the radius where the inner solution must be used, and thus the radius at which flattening becomes significant, increases with time ($r_{\rm flat} \propto \Omega_0^2 t^3$; TSC84).

The TSC84 solution is parameterized by the initial angular velocity of the core and the time since the formation of the protostar. We truncate the solution at the given $r_{\rm core}$ for each model and then renormalize the density profile so that the core mass matches the current $M_{\rm core}$ given by the hydro simulations. As in Paper II, we use the velocity profiles given by the TSC84 solution to allow $r_{\rm core}$ to decrease once the infall radius[8] exceeds the initial outer radius. By renormalizing the density profile to match the current $M_{\rm core}$ given by the hydro simulations our model is not completely physically self-consistent. However, this choice preserves both the exact evolution of core mass with time given by the hydro simulations and the qualitative feature of the TSC84 solution that the effects of rotational flattening on the core density profile increase with both time and initial core rotation.

Following Paper II, the assumed disk structure follows a power law in the radial coordinate and a Gaussian in the vertical coordinate, with the density profile given by

$$\rho_{\rm disk}(s, z) = \rho_0 \left(\frac{s}{s_o}\right)^{-\alpha} \exp\left[-\frac{1}{2}\left(\frac{z}{H_s}\right)^2\right], \qquad (11)$$

where z is the distance above the midplane ($z = r\cos\theta$, with r and θ the usual radial and zenith angle spherical coordinates, respectively), s is the distance in the midplane from the origin ($s = \sqrt{r^2 - z^2}$), H_s is the disk scale height, and ρ_0 is the density at the reference midplane distance s_0. All parameters describing the dependence of H_s on s (and thus the flaring of the disk) are the same as in Paper II. We note that this adopted disk flaring is very similar to that found in the hydrodynamical simulations (see Figure 11 in Vorobyov & Basu 2010). On the other hand, the adopted gas surface density profile $\Sigma \propto r^{-1}$ is somewhat shallower than the $\Sigma \propto r^{-1.5}$ usually seen in hydrodynamical

[7] Following the convention adopted in both Papers I and II, radii pertaining to the core are denoted by lowercase r, while radii pertaining to either the star or disk are denoted by uppercase R.

[8] The infall radius is the radius within which the core is collapsing. It starts at the center and moves outward at the sound speed.

simulations of gravitationally unstable disks in the embedded phase of star formation. The density profile is truncated at $R_{\rm disk}$ and normalized so that the total mass matches $M_{\rm disk}$ given by the simulations. The inner radius of the disk is set equal to the dust destruction radius, calculated (assuming spherical, blackbody dust grains) as

$$R_{\rm disk}^{\rm in} = \sqrt{\frac{L_*}{16\pi\sigma T_{\rm dust}^4}}, \quad (12)$$

where L_* is the protostellar luminosity (see below) and $T_{\rm dust}$ is the dust destruction temperature (assumed to be 1500 K; e.g., Cieza et al. 2005).

As in both Papers I and II, the total internal luminosity of the protostar and disk at each point in the collapse from core to star contains six components: (1) luminosity arising from accretion from the core directly onto the protostar, (2) luminosity arising from accretion from the core onto the disk, (3) luminosity arising from accretion from the disk onto the protostar, (4) disk "mixing luminosity" arising from luminosity released when newly accreted material mixes with existing disk material, (5) luminosity arising from the release of energy stored in differential rotation of the protostar, and (6) photosphere luminosity arising from gravitational contraction and deuterium burning. The first five components are calculated following Adams & Shu (1986); further details can be found in Papers I and II. In this work, however, the second and third components are calculated using direct input from the simulations, i.e., $\dot{M}_{\rm d}$ and $\dot{M}_{\rm s}$, respectively.

The sixth component, the photosphere luminosity arising from gravitational contraction and deuterium burning, follows the pre-main-sequence tracks of D'Antona & Mazzitelli (1994) with opacities from Alexander et al. (1989). In Papers I and II, an offset of 10^5 years was assumed between the onset of collapse and the zero time of these tracks (see also Myers et al. 1998). In this work, we take an improved approach by noting that the zero time of the D'Antona & Mazzitelli tracks corresponds to the time when deuterium burning begins in the protostellar interior. Hence, we make use of a simple stellar polytropic model and assume that the zero time of the pre-main-sequence tracks corresponds to the moment when the temperature in the stellar interior reaches 5×10^5 K. In order words, the time offset in our models is now the sum of two quantities: the time needed to form the first hydrostatic core from a pre-stellar cloud core, which may vary depending on the initial core mass, angular momentum, and density distributions, and the time needed to ignite deuterium burning in the forming central protostar, which is usually 2×10^4 yr after the first hydrostatic core formation.

Neither the time evolution of the protostellar radius nor that of the photosphere luminosity is included in our models in a self-consistent manner. $R_{\rm star}$ is calculated from $M_{\rm star}$ following Palla & Stahler (1991), who assume a constant accretion rate of $10^{-5}\,M_\odot$ yr^{-1}. The photosphere luminosity is included by adopting the pre-main-sequence tracks of D'Antona & Mazzitelli (1994). These tracks do not include accretion and suffer from the uncertainty of how to define the zero time relative to the onset of collapse and formation of the protostar. In reality, the accretion luminosity depends on the protostellar radius ($L_{\rm acc} \propto 1/R_{\rm star}$), and both the magnitude and zero time of the photosphere luminosity depend on the accretion history (Baraffe et al. 2009; Hosokawa et al. 2011; Hartmann et al. 2011). Thus, the accuracy of both components of the total model luminosity can be improved by including self-consistent calculations of the protostellar radius and photosphere luminosity. Such calculations can now be performed for any arbitrary accretion history (e.g., Baraffe et al. 2009) and will be explored in a future paper.

Finally, there is also external luminosity arising from heating of the core by the interstellar radiation field (ISRF). We adopt the same ISRF as Papers I and II: the Black (1994) ISRF, modified in the ultraviolet to reproduce the Draine (1978) ISRF, and then extincted by $A_V = 0.5$ of dust with properties given by Draine & Lee (1984) to simulate extinction by the surrounding lower density environment. We input the mean intensity of this ISRF ($J_{\rm ext}$) into the radiative transfer code as an additional source of heating. The luminosity added to $L_{\rm bol}$ from this external heating, $L_{\rm ext}$, is determined after each radiative transfer model is run by subtracting the total internal luminosity (the sum of the above six components) from the total model luminosity.

For each model, we use the two-dimensional, axisymmetric, Monte Carlo dust radiative transfer package RADMC (Dullemond & Turolla 2000; Dullemond & Dominik 2004) to calculate the two-dimensional dust temperature profile of the core throughout the duration of each model. Each model begins when the FHSC forms and terminates when 10% of the initial core mass remains, which we have taken to be the Class I/II boundary (Vorobyov 2009b; Vorobyov & Basu 2010). Some models with initially low core masses are extended until 1% of the initial core mass remains. The simulation output is resampled onto a time step grid appropriate for the radiative transfer models; a detailed description of this resampling and its effects on the results are given in the Appendix. For the dust properties, we adopt the dust opacities of Ossenkopf & Henning (1994) appropriate for thin ice mantles after 10^5 yr of coagulation at a gas density of 10^6 cm^{-3} (OH5 dust), which have been shown to be appropriate for cold, dense cores (e.g., Evans et al. 2001; Shirley et al. 2005). Isotropic scattering off dust grains is included in the model as described in Paper II. SEDs at each time step are then calculated at nine different inclinations ranging from $i = 5^\circ$–85° in steps of 10°. An inclination of $i = 0^\circ$ corresponds to a pole-on (face-on) system, while an inclination of $i = 90^\circ$ corresponds to an edge-on system.

3. COMPARING MODELS TO OBSERVATIONS

In this section, we briefly summarize the method we use to turn the models into observational signatures and the observational data set to which we compare the models. Further details can be found in Paper II.

3.1. Calculating Observational Signatures

We use the model SEDs to calculate observational signatures of the models at each time step for each inclination. We calculate the bolometric luminosity ($L_{\rm bol}$), the ratio of bolometric to submillimeter luminosity ($L_{\rm bol}/L_{\rm smm}$), and the bolometric temperature ($T_{\rm bol}$). $L_{\rm bol}$ is calculated by integrating over the full SED,

$$L_{\rm bol} = 4\pi d^2 \int_0^\infty S_\nu d\nu\,, \quad (13)$$

while the submillimeter luminosity is calculated by integrating over the SED for $\lambda \geqslant 350\,\mu$m,

$$L_{\rm smm} = 4\pi d^2 \int_0^{\nu=c/350\,\mu{\rm m}} S_\nu d\nu\,. \quad (14)$$

The bolometric temperature is defined to be the temperature of a blackbody with the same flux-weighted mean frequency as the

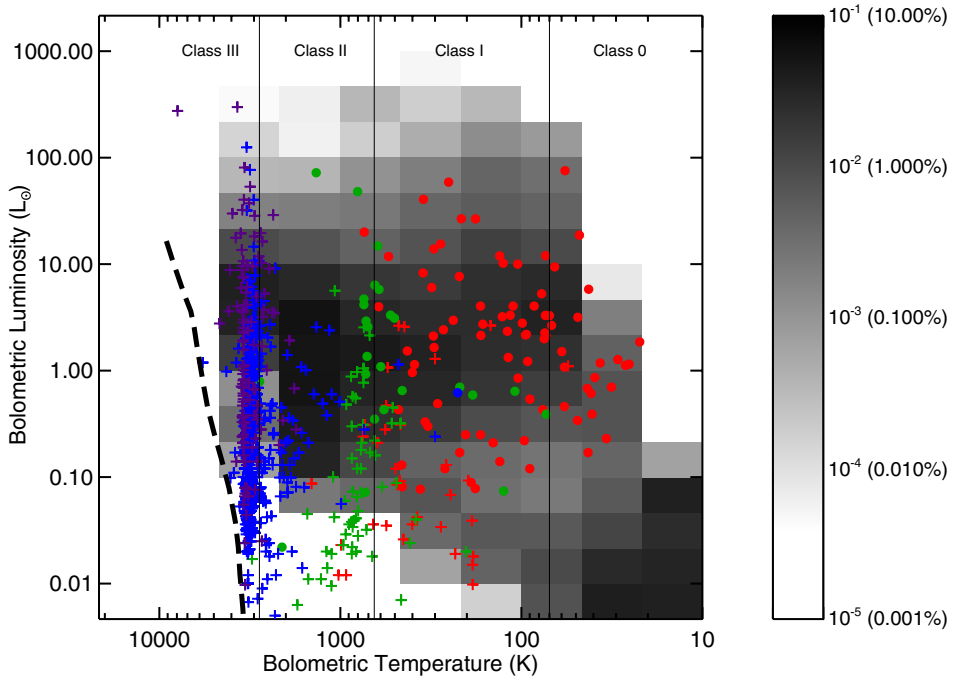

Figure 8. Combined BLT diagram for all models weighted by mass and inclination as described in the text. The gray-scale pixels indicate the fraction of total time the models spend in each $L_{\rm bol}$–$T_{\rm bol}$ bin, calculated from Equation (16). The gray scale is displayed in a logarithmic stretch with the mapping between gray scale and fraction of total time as indicated in the legend. The class boundaries in $T_{\rm bol}$ are taken from Chen et al. (1995). The thick dashed line shows the zero-age main sequence (ZAMS; D'Antona & Mazzitelli 1994) from 0.1 to 2.0 $M_\odot$. The colored symbols show the young stellar objects from Evans et al. (2009) in this diagram; the color indicates spectral class (red for Class 0/I, green for flat spectrum, blue for Class II, and purple for Class III), while a circle or cross indicates that the source is or is not, respectively, associated with a core as traced by millimeter continuum emission.

(A color version of this figure is available in the online journal.)

source (Myers & Ladd 1993). Following Myers & Ladd, $T_{\rm bol}$ is calculated as

$$T_{\rm bol} = 1.25 \times 10^{-11} \frac{\int_0^\infty \nu S_\nu d\nu}{\int_0^\infty S_\nu d\nu} \ {\rm K}. \quad (15)$$

$T_{\rm bol}$ can be thought of as a protostellar equivalent of $T_{\rm eff}$; $T_{\rm bol}$ starts at very low values ($\sim$10 K) for cold, starless cores and eventually increases to $T_{\rm eff}$ once the core and disk have fully dissipated. The integrals defined in Equations (13)–(15) are calculated using the trapezoid rule to integrate the finitely sampled model SEDs.

3.2. Observational Data Set

We use the 1024 young stellar objects (YSOs) in the five large, nearby molecular clouds surveyed by the *Spitzer Space Telescope* Legacy Project "From Molecular Cores to Planet Forming Disks" (Evans et al. 2003) as our observational data set. Evans et al. (2009) compiled photometry and calculated $L_{\rm bol}$ and $T_{\rm bol}$ for all 1024 YSOs in the same manner as described above after correcting the photometry for foreground extinction (see Evans et al. 2009 for details). They concluded that 112 of the 1024 YSOs are embedded protostars based on association with a millimeter continuum emission source tracing a core. Since the models presented here are those of cores collapsing to form protostars, it is to these 112 objects that we compare. Core masses for all objects in Perseus, Ophiuchus, and Serpens are taken from Enoch et al. (2009b).

4. RESULTS

Figure 8 compares the models considered here to observations by plotting $L_{\rm bol}$ versus $T_{\rm bol}$. Such a plot was first introduced by Myers et al. (1998), who called it a bolometric-luminosity–temperature (BLT) diagram, as a protostellar equivalent to the Hertzsprung–Russell diagram. Deeply embedded protostars surrounded by dense dust cores generally start at very low $L_{\rm bol}$ and $T_{\rm bol}$ and increase in both quantities as the dust core dissipates through accretion and mass loss and the source gains mass (and thus luminosity). $T_{\rm bol}$ eventually approaches $T_{\rm eff}$ as the surrounding dust fully dissipates. Indeed the stellar main sequence is plotted in Figure 8. Also plotted are the 1024 YSOs from Evans et al. (2009), with color indicating spectral class (red for Class 0/I, green for flat spectrum, blue for Class II, and purple for Class III; see Evans et al. for details) and symbol indicating source type (circles for sources associated with envelopes as traced by millimeter continuum emission, plus signs for sources not associated with envelopes).

To compare the models and observations, we determine the fraction of total time the models spend in various bins in the BLT diagram. To calculate this fraction, we first divide the $L_{\rm bol}$–$T_{\rm bol}$ space into bins of 1/3 dex in both dimensions and then calculate the fraction of total time the models spend in each $L_{\rm bol}$–$T_{\rm bol}$ bin ($f_{\rm bin}$) as

$$f_{\rm bin} = \frac{\sum_{\rm mass} \left(\sum_{\rm inc} t_{\rm bin} w_{\rm inc} \right) w_{\rm mass}}{\sum_{\rm mass} \left(\sum_{\rm inc} t_{\rm model} w_{\rm inc} \right) w_{\rm mass}}, \quad (16)$$

where the numerator is the time spent in the bin and the denominator is the total time. The interior sum in both the numerator and denominator is over the nine different inclinations while the exterior sum is over the different initial core masses. The quantity $t_{\rm bin}$ is the total time that a particular model viewed at a particular inclination spends in the specified $L_{\rm bol}$–$T_{\rm bol}$ bin

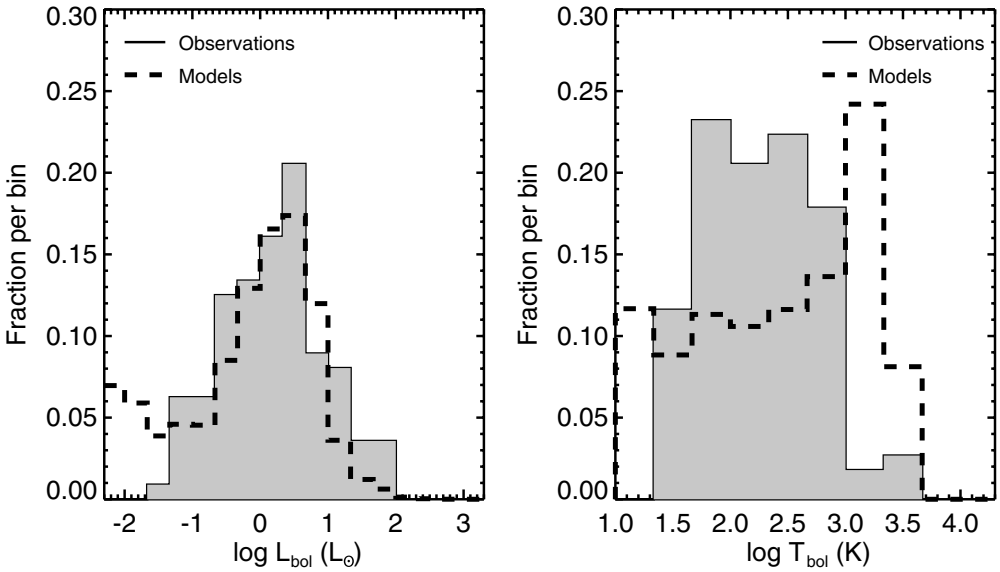

Figure 9. Histograms showing the fraction of total sources (observations; solid filled histogram) and fraction of total time spent by all models (dashed unfilled histogram; calculated from Equation (16)) at various $L_{\rm bol}$ (left) and $T_{\rm bol}$ (right). The bin size is 1/3 dex in both quantities. For the observations, only the 112 embedded sources (plotted as filled circles on the BLT diagrams) are included.

whereas $t_{\rm model}$ is the total duration of each individual model. $w_{\rm inc}$ is the weight each inclination receives in the sum, defined as the fraction of solid area subtended by that inclination. As in Paper II, this is calculated in practice by assuming each of the nine SEDs calculated is valid for inclinations spanning the range $(i - 5^\circ)$ to $(i + 5^\circ)$.

The final quantity in Equation (16) is $w_{\rm mass}$, the weight given to each of the individual models. In Paper II, we assigned these weights according to the initial core mass and the empirically derived core mass function (CMF) of starless cores (Motte et al. 1998; Testi & Sargent 1998; Johnstone et al. 2000, 2001; Motte et al. 2001; Johnstone & Bally 2006; Alves et al. 2007; Nutter & Ward-Thompson 2007; Enoch et al. 2008; Hatchell & Fuller 2008; Simpson et al. 2008; Rathborne et al. 2009; Sadavoy et al. 2010). However, as noted in Paper II, there is considerable variation in the CMF between the various studies cited above, particularly below an initial core mass of $\sim 1\,M_\odot$ since most of these studies feature completeness limits between 0.1 and 1 $M_\odot$. Thus, in this paper we instead assign the weights according to the final stellar mass produced by each model and the stellar IMF. We adopt the Kroupa (2002) three-component power-law IMF, which gives $dN/dM \propto M^{-\alpha}$, with $\alpha = 0.3$ for $0.01 \leqslant M/M_\odot < 0.08$, $\alpha = 1.3$ for $0.08 \leqslant M/M_\odot < 0.5$, and $\alpha = 2.3$ for $M/M_\odot \geqslant 0.5$. As noted by Kroupa (2002), the IMF may actually be better described by a four-component power law, with $\alpha = 2.7$ for $M/M_\odot \geqslant 1$ if uncertain corrections for unresolved multiple systems are applied. As these corrections are very uncertain we do not adopt them here.

With the fraction of total time spent in each bin in the BLT diagram calculated as described above, we plot the results as gray-scale pixels in Figure 8. Since the models span only the duration of the embedded stage when the protostar and disk are still surrounded by the dense core from which they are forming, the relevant comparison is to the 112 embedded sources associated with cores as traced by millimeter continuum emission and thus plotted as filled circles. The models clearly reproduce the full spread of observations of embedded sources in this diagram, unlike models with constant mass accretion, which only reproduce the high luminosity end of this spread (see, e.g., Figure 19 of Paper I and Figures 1, 7, 11, and 16 of Paper II). While at first glance it appears that the models overpredict the fraction of total time at high luminosities compared to the observations, this is an artifact of the logarithmic scaling. The models only spend 0.2% of the time above 100 $L_\odot$; in a data set of 112 protostars, there should be <1 object at such high luminosities, consistent with the observations.

We also compare the models to the observed $L_{\rm bol}$ and $T_{\rm bol}$ distributions separately in Figure 9. The observational histograms in Figure 9 only include the 112 embedded sources associated with envelopes (plotted as filled circles in Figure 8) and plot the fraction of total sources in each bin, while the model histograms plot the fraction of total time spent in each bin calculated from Equation (16). The left panel of Figure 9 shows that the models generally reproduce the observed protostellar luminosity distribution; a K-S test on the observed and model $L_{\rm bol}$ distributions returns a value of 0.85, indicating that the two distributions are quite similar. Most of the difference between the model and observed distributions actually exists in a "reverse luminosity problem," a point we will return to in Section 5.1. The right panel suggests that the models do not provide as good a match to the observed $T_{\rm bol}$ distribution; a K-S test on the observed and model $T_{\rm bol}$ distributions returns a value of 0.42, confirming this observation. Most of the difference is in a population of embedded objects at high $T_{\rm bol}$ ($\gtrsim$1000 K) predicted by the models but lacking in the observations. We will discuss this discrepancy in detail in Section 5.2 below, but note here the main point that this discrepancy does not affect our conclusions regarding the match between observed and model luminosities.

Figure 10 compares the models and observations on a plot of $L_{\rm bol}$ versus $M_{\rm core}$. The filled circles show the same embedded sources as in Figure 8, with color again indicating spectral class. The core masses could easily shift by factors of ~2–4 in both directions depending on the true values of the dust opacity (e.g., Shirley et al. 2005, 2011) and dust temperature in each core. Furthermore, both $L_{\rm bol}$ and $M_{\rm core}$ have variable completeness limits since the star-forming regions surveyed by c2d are not all located at the same distance. Even for sources

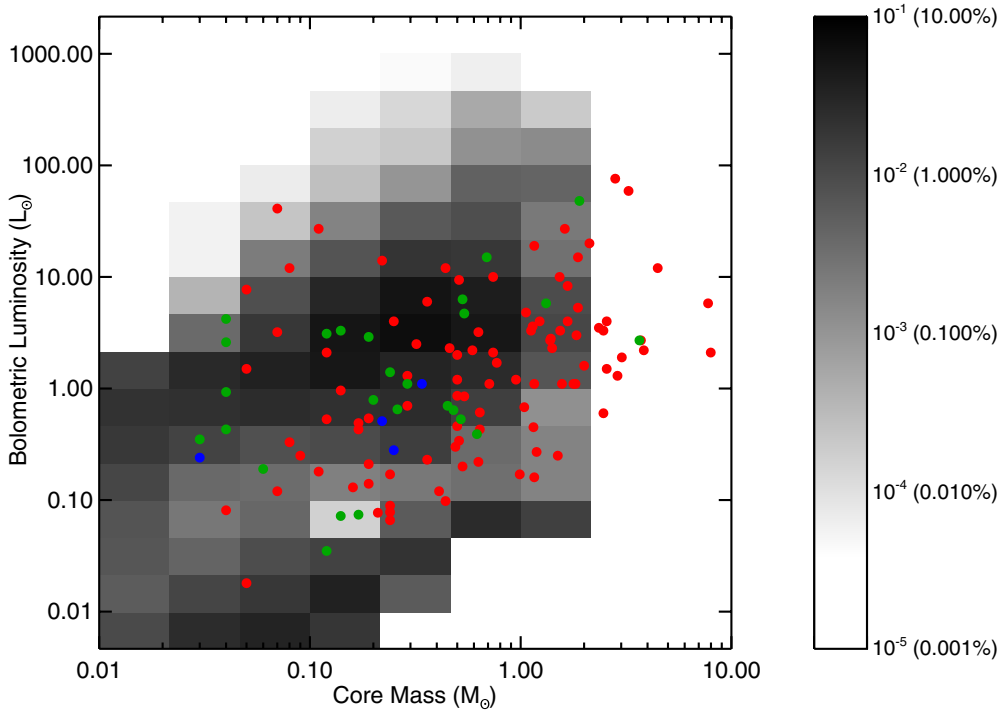

Figure 10. Combined plot of $L_{\rm bol}$ vs. $M_{\rm core}$ for all models weighted by mass and inclination as described in the text. The gray-scale pixels indicate the fraction of total time the models spend in each $L_{\rm bol}$–$M_{\rm core}$ bin, calculated from Equation (16). The gray scale is displayed in a logarithmic stretch with the mapping between gray scale and fraction of total time as indicated in the legend. The colored symbols show the young stellar objects from Evans et al. (2009) in this diagram, with $M_{\rm core}$ taken from Enoch et al. (2009b) and the color is used to indicate the spectral class (red for Class 0/I, green for flat spectrum, blue for Class II, and purple for Class III). (A color version of this figure is available in the online journal.)

at the same distance the completeness limits are difficult to quantify with a single number. For $L_{\rm bol}$, the c2d survey is generally complete to protostars with $L_{\rm bol} \gtrsim 0.05\ L_\odot$, although the exact completeness limit varies depending on the detailed shape of the SED of each source (Dunham et al. 2008; Evans et al. 2009; Enoch et al. 2009b). For $M_{\rm core}$, the observations presented by Enoch et al. (2009b) are generally complete above $0.8\ M_\odot$, but the exact completeness limit depends on core size due to observing and data reduction limitations (see Enoch et al. 2008 for details). Thus, we simply note that the models do appear to reproduce the full spread of sources in $L_{\rm bol}$–$M_{\rm core}$ space, including the existence of VeLLOs with $L_{\rm bol} \sim 0.1$–$0.2\ L_\odot$ and $M_{\rm core} \sim 1\ M_\odot$.[9] This diagram should be revisited in the future once deeper submillimeter and millimeter continuum surveys of nearby star-forming regions (such as the upcoming SCUBA-2 Gould Belt survey; Ward-Thompson et al. 2007b) have been completed to evaluate whether or not the time spent at $L_{\rm bol} \lesssim 1\ L_\odot$ and $M_{\rm core} \lesssim 0.1\ M_\odot$, as predicted by the models, is matched by observations of embedded sources.

5. DISCUSSION

5.1. Resolving the Luminosity Problem

As shown above in Figures 8 and 9, the models considered here reproduce the full range of observations in $L_{\rm bol}$–$T_{\rm bol}$ space and provide a reasonable match to the observed protostellar luminosity distribution. Thus we conclude that the accretion process predicted by the Vorobyov & Basu (2005b, 2006, 2010) simulations of collapsing cores resolves the luminosity problem, although we caution that these results must be revisited in the future once simulations that feature smaller sink cells closer to the stellar surface and fully capture both the physics in the inner disk and the actual protostellar accretion rates are possible (see Section 2.1.3 for further discussion). In Paper II, we argued that episodic accretion is both necessary and sufficient to resolve the luminosity problem, but this conclusion is subject to uncertainty since the actual prescription for episodic accretion included in that paper was quite simple and did not fully capture the accretion process in the simulations. Here we have coupled the exact evolution of the collapsing cores with radiative transfer calculations and demonstrated that the Vorobyov & Basu simulations resolve the luminosity problem, although we defer the question of whether or not episodic accretion itself is necessary to Section 5.4 below. We also note here that these models predict a smooth distribution in $L_{\rm bol}$–$T_{\rm bol}$ space, whereas the models in Paper II featured white "excluded zones" where the models spent no time but sources were observed to exist. The fact that only three initial mass cores were considered in Paper II (0.3, 1, and 3 $M_\odot$) was argued to artificially create these zones; the increased sampling of core masses in this paper confirms this argument.

Most of the remaining discrepancy between the model predictions and observations of protostellar luminosities actually appears in the form of a "reverse luminosity problem," evident in both Figures 8 and 9 as an overabundance of time spent at $L_{\rm bol} \lesssim 0.1\ L_\odot$ compared to observations. Indeed, a K-S test on the observed and model luminosity distributions that only compares the distributions above $0.1\ L_\odot$ returns a value of 0.87, slightly higher than the value of 0.85 obtained for the full distributions. What causes the disagreement at low luminosities? Only 7% of the observed sources have $L_{\rm bol} \leqslant 0.1\ L_\odot$

[9] As stated in Section 1, a VeLLO is, by definition, a protostar with $L_{\rm int} \leqslant 0.1\ L_\odot$, but external heating will raise $L_{\rm bol}$ to higher values. For example, the VeLLO IRAM04191 + 1522 has $L_{\rm int} \sim 0.08\ L_\odot$ but $L_{\rm bol} \sim 0.15\ L_\odot$ (André et al. 1999; Dunham et al. 2006).

whereas the models spent 21% of the total time at such luminosities. Furthermore, the majority of this time (19% out of 21%) is spent at $T_{\rm bol} \leqslant 100$ K, where there are no observed sources. At least some, and possibly all, of this discrepancy can be explained by observational completeness limits. As noted above, the c2d survey is generally complete to protostars with $L_{\rm bol} \gtrsim 0.05\ L_{\odot}$, although the exact completeness limit varies depending on distance and the detailed shape of the SED of each source. Indeed, several extremely low luminosity sources undetected in the *Spitzer* c2d survey, with both internal and bolometric luminosities significantly below 0.1 $L_{\odot}$, have recently been discovered, most through detections of outflows driven by cores with no associated *Spitzer* c2d sources (Chen et al. 2010; Enoch et al. 2010; Dunham et al. 2011; Pineda et al. 2011). With such low luminosities at least some of these sources may be first hydrostatic cores. Sensitive interferometer outflow surveys and very deep *Herschel* and *James Webb Space Telescope* infrared surveys directed toward cores currently classified as starless are needed to fully identify and characterize the population of such extremely low luminosity protostars and/or first cores before an accurate comparison to the models can be made for luminosities below 0.1 $L_{\odot}$.

5.2. Bolometric Temperatures

As noted above in Section 4, the models do not provide a good match to the observed $T_{\rm bol}$ distribution, with most of the discrepancy in a population of embedded objects at high $T_{\rm bol}$ ($\gtrsim$1000 K) predicted by the models but lacking in the observations. In the models, most of this time spent at $T_{\rm bol} \gtrsim 1000$ K arises when $R_{\rm disk}$ is larger than a few hundred AU and the line of sight does not pass through the disk. As described in detail in Section 2.2, we adopt analytic profiles for the disk and core density profiles since the hydro simulations do not provide the full vertical density structure. In order to do this, we define the core inner radius to be equal to the disk outer radius so that there is no overlap between where the disk and core density profiles are defined. However, as a consequence of this method, large cavities devoid of material exist above the surface of the disk but within the core inner radius, and these cavities increase as the disk sizes increase. Lines of sight that pass through these cavities have reduced optical depths, allowing more short-wavelength emission to escape and thus increasing $T_{\rm bol}$.

In reality, such large cavities are unlikely to exist; instead, the disk and core density profiles should smoothly join together. As we have mentioned in Section 2.2, an improved methodology that reconstructs the disk and core vertical structure and incorporates this exact structure into the radiative transfer calculations (rather than adopting simple analytic profiles) is currently under development and will be presented in a future paper. This method will result in a more accurate distribution of material above the disk surface and will likely remove much of the discrepancy between observed and model values of $T_{\rm bol}$. Since the distribution of luminosities is set mainly by the accretion rates and protostellar masses, we argue that including a more accurate physical structure should not significantly alter our results on the resolution of the luminosity problem, although this will be explicitly tested in a future paper. We also note here the possibility that these models contain too much rotation and angular momentum, since this would cause both the rotational flattening of the cores and sizes of the disks to be overestimated, resulting in the models overpredicting $T_{\rm bol}$ compared to observations. As discussed in some detail in Section 2.1.2 above, we do not consider this to be very likely, but we acknowledge that it is a possibility since β, the ratio of rotational to gravitational energy, is not a directly observable quantity and observed ranges of β could be overestimated if infall and/or outflow motion is mistakenly attributed to rotation.

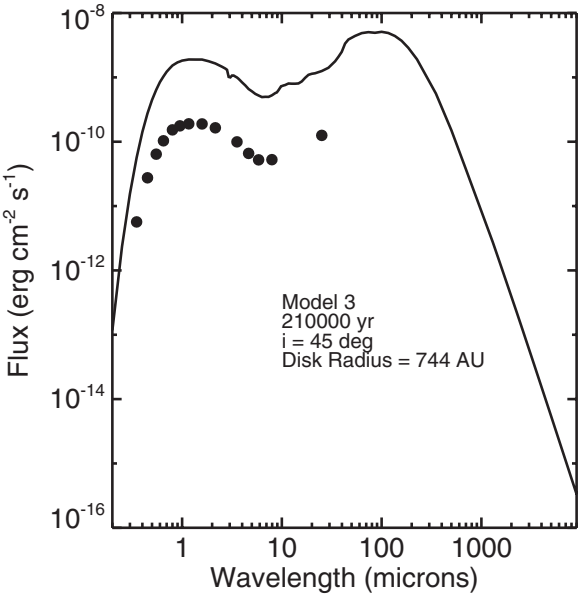

Figure 11. Example of a spectral energy distribution (SED) for a model with high $T_{\rm bol}$. This particular SED is for the $i = 45^{\rm o}$ line of sight at 210,000 yr into the collapse of model 3, when the core mass is 0.9649 $M_{\odot}$, the disk mass is 0.1656 $M_{\odot}$, the protostellar mass is 0.5122 $M_{\odot}$, and the disk radius is 744 AU. This SED has $T_{\rm bol} = 1037$ K. The solid line plots the model SED over all wavelengths, while the points show the model SED at standard optical and near-infrared wavelengths and the 3.6–70 μm wavelengths provided by the *Spitzer Space Telescope*. The points have been shifted down by a factor of 10 for clarity.

Even after including a more accurate physical structure, some discrepancy between observed and model values of $T_{\rm bol}$ may remain, particularly once the effects of outflow cavities are included. Figure 11, which plots an example SED for a model with high $T_{\rm bol}$, shows that such models feature a double-peaked SED. This figure also demonstrates that, from optical wavelengths to either the 24 or 70 μm bands probed by *Spitzer* observations, such models resemble transition disk Class II sources (sometimes also referred to as cold disk sources; see Merín et al. 2010 and references therein). Given that our models predict that 40% of embedded sources are classified as Class II by $T_{\rm bol}$, and that the observed fraction of Class 0+I to Class II sources is 0.19 when classifying via extinction-corrected values of $T_{\rm bol}$ (Evans et al. 2009), our models predict that 12% of Class II YSOs are actually embedded objects with SEDs like that shown in Figure 11. While this is consistent with the upper range of the observed fraction of Class II sources with transition disk SEDs (3%–12%; Merín et al. 2010; Furlan et al. 2011), the models clearly overpredict this fraction, as described above. Nevertheless, we caution that a small fraction of Class II sources with transition disk SEDs could in fact be embedded sources.

If the above statement is true, why are they missing from the observed sample of embedded sources? As discussed in detail in Paper II, whether or not a population of embedded objects with high $T_{\rm bol}$ exists remains an open question. The Evans et al. (2009) sample is based primarily on the association of *Spitzer* sources featuring rising SEDs and red colors with millimeter continuum sources (Enoch et al. 2009b; Dunham et al. 2008) and is likely biased against such objects since they would often

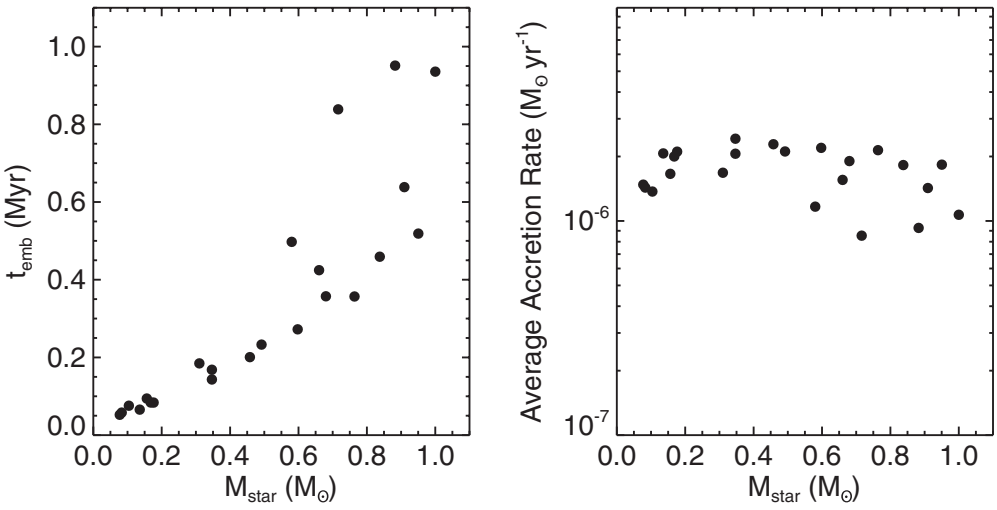

Figure 12. Left: $t_{\rm emb}$ vs. $M_{\rm star}$ for the 23 models listed in Table 1 and considered in this paper. Right: average $\dot{M}_s$ over the embedded phase duration vs. $M_{\rm star}$ for the same models.

not meet these criteria and would instead be assumed to be chance alignments between millimeter continuum sources and background sources and/or later-stage YSOs. Furthermore, the extinction corrections applied by Evans et al. (2009) to the embedded sources are average extinctions over each individual cloud rather than true line-of-sight extinctions, and thus may underestimate the true extinction since current, active star formation (and thus the position of the youngest, embedded sources) is associated with the densest parts of molecular clouds (e.g., Heiderman et al. 2010; Lada et al. 2010). As shown in Paper II, such underestimates could, in the worst cases, artificially lower $T_{\rm bol}$ from several thousand K to several hundred K. Future work must revisit the observational samples and carefully evaluate whether or not a population of embedded sources with high enough $T_{\rm bol}$ to be classified as Class II or Class III exists.

5.3. Duration of the Embedded Phase

For the 23 models listed in Table 1 and considered in this paper, the duration of the embedded phase ($t_{\rm emb}$) ranges from 0.052 (model 19) to 0.951 Myr (model 11). For each model, Figure 12 plots both $t_{\rm emb}$ (left panel) and the average accretion rate over the embedded phase duration (right panel, calculated as final stellar mass divided by $t_{\rm emb}$) versus the final stellar mass produced by the model. The duration of the embedded phase increases approximately linearly with the final stellar mass produced, and thus the average mass accretion rate (not to be confused with the *instantaneous* mass accretion rate, which is highly variable; see Figure 2) is approximately constant and does not depend on final stellar mass. Offner & McKee (2011) argued that models that tend toward constant accretion time rather than constant accretion rate are necessary to match the observed protostellar luminosity distribution, consistent with the conclusion by Myers (2010) that accretion rates that increase with mass can at least partially resolve the luminosity problem. We disagree that such models are necessary. Our models tend toward a constant average accretion rate of $\sim$1–3 $\times$ 10^{-6} $M_\odot$ yr^{-1} rather than a constant accretion time yet still provide an excellent match to the observed protostellar luminosity distribution.

The average duration of the embedded phase, weighted by final stellar mass as described in Section 4, is 0.12 Myr. In contrast, Evans et al. (2009) derived an embedded phase lifetime of $t_{\rm emb}$ = 0.44 Myr based on the ratio of Class 0+I sources to Class II sources in the c2d sample and the assumption of a Class II lifetime of 2 Myr. Thus, these models predict a significantly shorter $t_{\rm emb}$ than suggested by recent observations. However, a number of caveats apply to this comparison: (1) we have taken the Class I/II boundary to be the point at which 10% of the initial core mass remains and terminate the models at this point. In reality the exact point at which to set this class boundary is uncertain and could easily shift the duration of the embedded phase by factors of $\sim$2 in either direction; (2) the observationally determined $t_{\rm emb}$ is pinned to a Class II lifetime of 2 Myr, but the uncertainty in this lifetime is about 1 Myr (50%; see discussion in Evans et al. 2009); and (3) the number of Class 0+I sources in the Evans et al. sample may be overestimated.

The third point above is emphasized by three recent studies. First, van Kempen et al. (2009) observed 22 Class I sources in Ophiuchus in HCO$^+$ J = 4–3, a tracer of warm and dense gas, and showed that 11 (50%) are not detected and thus show no evidence of being surrounded by a dense core. Second, McClure et al. (2010) used their revised extinction law and classification method to show that greater than 50% of the Class I sources in Ophiuchus are highly extincted disk sources no longer embedded within cores. Third, Heiderman et al. (2010) observed 53 Class I sources in a variety of nearby star-forming regions in HCO$^+$ J = 3–2, a tracer of dense gas, and showed that 31 (58%) are not detected and thus not associated with a dense core. All three studies likely represent upper limits to the true fraction of "fake" Class I sources. In the cases of van Kempen et al. (2009) and McClure et al. (2010) this is because there is substantial evidence that Ophiuchus is located behind an extinction screen that, if not properly accounted for, will redden source SEDs and artificially increase the number of Class I sources (see, e.g., Figure 12 of Evans et al. 2009). In the case of Heiderman et al. (2010) this is because their study specifically targeted suspicious Class I sources located in low extinction regions of clouds. We thus consider 50% as an upper limit to the fraction of Class I sources in the Evans et al. (2009) sample that are actually misclassified Class II sources. Shifting 50% of the Class I sources to Class II would decrease the Evans et al. (2009) observationally determined value of $t_{\rm emb}$ from 0.44 Myr to 0.2 Myr. Combined with the other caveats mentioned above,

the duration of the embedded phase predicted by our models is marginally consistent with observations but should be revisited in the future as uncertainties in the observations are improved.

Finally, the Stage 0 ($[M_{\rm star}+M_{\rm disk}]/[M_{\rm star}+M_{\rm disk}+M_{\rm core}] \leqslant 0.5$; André et al. 1993) duration for the 23 models considered in this paper ranges from 0.009 Myr (model 19) to 0.256 Myr (model 15), with an average (again weighted by final stellar mass as described in Section 5) of 0.027 Myr. Compared to the total embedded duration of 0.12 Myr, our models predict that the Stage 0 phase is only 23% of the total embedded duration. This is a natural consequence of the fact that these models feature average mass accretion rates that decrease with time (Vorobyov & Basu 2010; see Figure 2), thus the first 50% of the mass will accrete from the core faster than the second 50% of the mass. Our results are generally consistent with recent observationally determined estimates of the lifetime of Stage 0 relative to the total embedded phase. For example, Enoch et al. (2009b) found 39 Class 0 and 89 Class I sources in Perseus, Ophiuchus, and Serpens, giving a relative Stage 0 lifetime of 30% of the total embedded phase duration. Additionally, Maury et al. (2011) found that between 9 and 12 of the 57 protostars they identified in the Serpens South cluster (Gutermuth et al. 2008) were Class 0 sources, giving a relative Stage 0 lifetime of 16%–21% of the total embedded phase duration. While the Enoch et al. and Maury et al. results are difficult to compare quantitatively since they use different classification methods that trace the underlying physical stage to different degrees of accuracy ($T_{\rm bol}$ in the case of Enoch et al. and position in $L_{\rm bol}$–$M_{\rm core}$ space in the case of Maury et al.), the general agreement between our models and these observational results is encouraging.

5.4. Number, Duration, and Importance of Bursts

The 23 models considered in this paper feature between 0 (model 16) and 97 (model 15) accretion bursts, where the exact criteria for defining bursts are given in the Appendix. The percentage of total time spent in bursts ranges from 0% (model 16) to 11.8% (model 15), and the percentage of total mass accreted in bursts ranges from 0% (model 16) to 35.5% (model 4). On average (where the average is weighted by final stellar mass as described in Section 4), 1.3% of the total time is spent in bursts and 5.3% of the total mass is accreted in these bursts. These values represent the statistical average values of the fraction of total time spent and mass accreted in bursts assuming a standard Kroupa IMF (see Section 4 for details). We caution that the exact values depend on the criteria used for defining bursts and would increase if a lower accretion rate floor were used (see the Appendix).

The simple, parameterized models presented in Paper II spend between 1.5% and 2% of their total time in bursts, consistent with the 1.3% of total time featured by these models. However, in the Paper II models between 50% and 91% of the final stellar mass accretes in bursts, in stark contrast to the 5.3% of total mass that accretes in bursts in the models considered here. The explanation for this large difference lies in the detailed implementation of accretion bursts in Paper II. As described in Section 1, a burst was triggered each time the ratio of $M_{\rm disk}$ to $M_{\rm star}$ exceeded 0.2. At this point the accretion rate onto the star was increased from 0 $M_\odot$ yr^{-1} to 10^{-4} $M_\odot$ yr^{-1} until the disk was fully drained of mass, allowing the cycle to begin anew. However, in reality only the most extreme bursts reach accretion rates of $10^{-4} M_\odot$ yr^{-1}, as evident from Figure 2. Furthermore, only a very small amount of the mass in the disk accretes in a given burst (about 10^{-2} $M_\odot$on average), whereas in Paper II the assumption that the disk was fully drained in each burst led to situations where up to 0.1–0.2 $M_\odot$ were accreting in single bursts. The models considered here, based on actual hydrodynamic simulations rather than simple parameterizations, are significantly more realistic.

Comparison to the results presented in Papers I and II demonstrates that the accretion process predicted by the Vorobyov & Basu (2005b, 2006, 2010) simulations essentially resolves the luminosity problem inherent in models with constant mass accretion. As first noted by Kenyon et al. (1990), there are two types of non-steady mass accretion that could potentially resolve the luminosity problem: (1) accretion rates that start high and then decrease with time, and (2) generally low accretion rates punctuated by short, episodic bursts of high accretion. Figure 2 clearly illustrates that the Vorobyov & Basu simulations feature both declining accretion rates with time *and* short, episodic accretion bursts. Which of these is responsible for resolving the luminosity problem?

Given that, on average, only 5.3% of the total mass accretes in bursts, one might suspect that it is the declining accretion rates with time rather than the bursts that lower model luminosities and improve the match to observations. However, this 5.3% excludes all of the mass that accretes in lower-amplitude accretion rate increases that do not meet the criteria for a burst as defined in the Appendix. Thus, to properly evaluate whether the bursts are required in order to resolve the luminosity problem, we have time-averaged the accretion rates to filter out the effects of the bursts and variability and re-run all 23 models. We averaged all models over 20,000 yr durations unless the total model duration was less than 0.2 Myr, in which case we decreased the averaging window to either 10,000 or 5000 yr in order to preserve at least 10 time steps between the formation of the protostar and the end of the embedded phase.

Figure 13 plots histograms comparing the fraction of total time the time-averaged models spend at various $L_{\rm bol}$ and $T_{\rm bol}$ to the observed distributions, similar to Figure 9. While the time-averaged models provide a much better match to observations than models with constant mass accretion (see Papers I and II for such models), comparing Figures 9 and 13 shows that the time-averaged models feature a small shift to higher luminosities and do not do quite as good of a job resolving the luminosity problem. This is confirmed by a K-S test on the observed and time-averaged model luminosity distributions, which returns a value of 0.59, lower than the value of 0.85 returned for the original models.

These results indicate that the declining accretion rates are not solely responsible for resolving the luminosity problem, a finding that is only reinforced by the fact that, even with the large windows over which we have time-averaged, the variability and bursts are not fully filtered out[10] (see Figure 14 for an example). We thus conclude that it is a combination of both the accretion rates that decline with time and the variability and episodic bursts that resolve the luminosity problem. We consider this to be a plausible result given that the Vorobyov & Basu simulations self-consistently predict both, and we argue that the fact that the bursts are required is in general agreement with the other indirect evidence for accretion variability and bursts described in Section 1.

[10] In theory we could adopt even larger averaging windows, but to do so would decrease the total number of time steps below 10 for many models and risk not fully sampling the decline of the accretion rate with time.

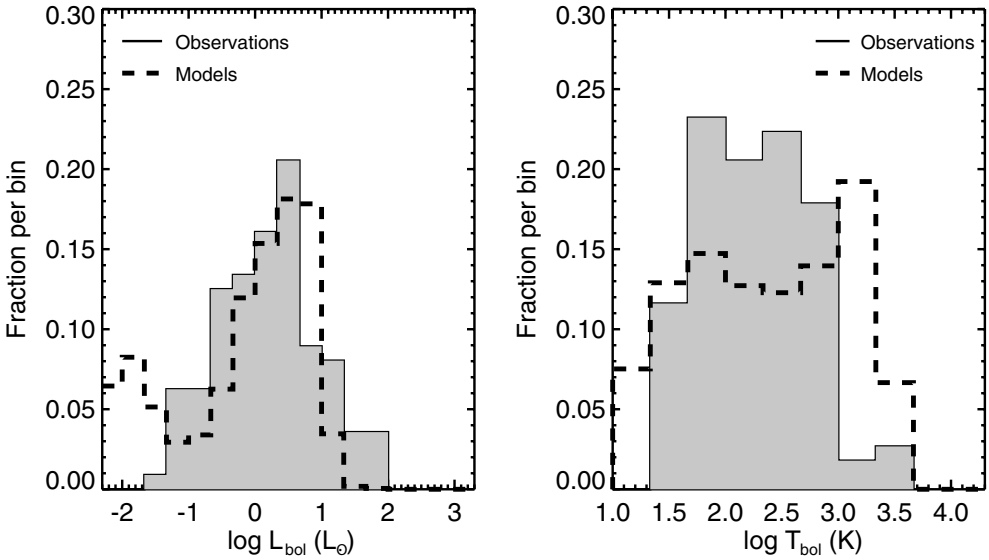

Figure 13. Histograms showing the fraction of total sources (observations; solid filled histogram) and fraction of total time spent by all models after time-averaging as described in Section 5.4 (dashed unfilled histogram; calculated from Equation (16)) at various $L_{\rm bol}$ (left) and $T_{\rm bol}$ (right). The bin size is 1/3 dex in both quantities. For the observations, only the 112 embedded sources (plotted as filled circles on the BLT diagrams) are included.

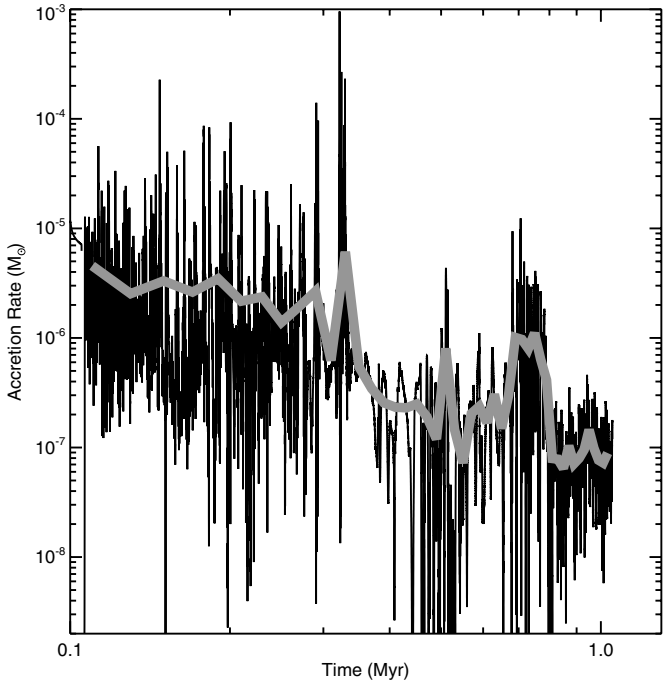

Figure 14. $\dot{M}_s$ vs. time for the original (thin black line) and time-averaged (thick gray line) time steps for model 11. A window of 20,000 yr was used for the time-averaging. Note that the variability and bursts have not been fully filtered out.

6. SUMMARY

In this paper, we have coupled radiative transfer models with hydrodynamical simulations of collapsing cores predicting accretion rates that both decline with time and feature episodic accretion bursts caused by fragments torqued onto the protostar. We have calculated the time evolution of standard observational signatures ($L_{\rm bol}$, $T_{\rm bol}$, and $L_{\rm bol}/L_{\rm smm}$) for cores collapsing following these simulations. We have compared our results to a database of 1024 YSOs containing 112 embedded protostars recently compiled by Evans et al. (2009). We summarize our main conclusions as follows.

1. The hydrodynamical simulations presented by Vorobyov & Basu (2005b, 2006, 2010) reproduce the full spread of observed embedded protostars in a diagram of $L_{\rm bol}$ versus $T_{\rm bol}$. The models resolve the luminosity problem and provide a reasonable match to the observed protostellar luminosity distribution (K-S value of 0.85). The models predict a large number of sources at very low ($\lesssim$0.1 $L_\odot$) luminosities absent in the observations due to the observational sensitivity limit; removing such low luminosities from the comparison between models and observations increases the K-S value to 0.87. The models predict that only 0.2% of the total time is spent at $L_{\rm bol} \geqslant 100\,L_\odot$; a larger data set than the 112 protostars considered here is necessary to test this prediction. Time-averaged models that filter out the accretion variability and bursts do not provide as good of a match to the observed luminosity problem, suggesting that the bursts are required.
2. The models do not provide a good match to the distribution of observed $T_{\rm bol}$ for embedded protostars (K-S value of 0.42). Instead, the models predict a substantial population of embedded protostars at $T_{\rm bol} \gtrsim 1000$ K and thus classified as Class II or Class III sources. Most of this discrepancy arises from the method by which we adopted analytic disk and core density profiles and will be alleviated with future models that incorporate the exact physical structure from the hydro simulations, but some of the discrepancy may also be due to a population of embedded protostars with high values of $T_{\rm bol}$ missing from the current database of protostars due to the selection criteria applied to construct this database. The planned future models will not significantly alter the model luminosity distribution since this is primarily determined by the accretion rates and protostellar masses, not by the detailed physical structure adopted in the radiative transfer calculations.
3. The models reproduce the full spread of sources in a plot of $L_{\rm bol}$ versus $M_{\rm core}$, including the existence of very low luminosity protostars with $L_{\rm bol} \sim 0.1$–$0.2\,L_\odot$ but relatively high core masses of 1–2 $M_\odot$.
4. The duration of each model is approximately proportional to the final stellar mass produced, yet these models resolve

the luminosity problem and provide an excellent match to the observed protostellar luminosity distribution. This is in contrast to recent results in the literature claiming that models that tend toward constant accretion time rather than constant accretion rate are necessary to match the observed distribution.

5. The IMF-weighted average duration of the embedded phase in our models is 0.12 Myr, whereas Evans et al. (2009) recently determined the embedded phase duration to be 0.44 Myr. We have suggested a number of possible means by which these two estimates of the embedded phase duration may be reconciled. The IMF-weighted average model Stage 0 duration is 0.027 Myr, or 23% of the total embedded phase duration. Observationally determined values based on the ratio of Class 0 to Class I sources range from 16% to 30% (Enoch et al. 2009b; Maury et al. 2011). Our models are consistent with this range.
6. On average, these models spend 1.3% of their total time in accretion bursts during which time 5.3% of the final stellar mass accretes. In the most extreme models these values reach 11.8% and 35.5%, respectively. Thus, accretion is not truly "episodic" since it actually occurs at all times rather than only in episodes. A better description is that accretion is "variable with episodic bursts."

Future work must concentrate on improving the accuracy and self-consistency of the hydrodynamical simulations and radiative transfer models, and on compiling a more complete and more accurate database of protostars and their observational signatures. Nevertheless, we expect our primary conclusion that the Vorobyov & Basu (2005b, 2006, 2010) simulations resolve the luminosity problem and match the observed protostellar luminosity distribution to remain unchanged to such future improvements.

We thank the referee for a careful reading of this paper and several comments that have significantly improved the quality of this work. We also thank Neal Evans, Stella Offner, and Chris McKee for reading a draft of this paper in advance of publication and providing helpful comments and questions. Support for this work was provided by JPL contract 1433171 and RFBR grants 10-02-00278 and 11-02-92601. M. M. Dunham acknowledges travel support from an International Travel Grant from the AAS, and E. I. Vorobyov acknowledges support from a Lise Meitner fellowship. The authors gratefully acknowledge N. J. Evans at The University of Texas at Austin for hosting both M. M. Dunham and E. I. Vorobyov at UT Austin to begin work on this project. Support for this visit was provided by NSF grant AST-0607793 to N. J. Evans and the UT Austin Tinsley Visitor's Fund. This research has made use of NASA's Astrophysics Data System Bibliographic Services.

APPENDIX

RESAMPLING TIME STEPS

The simulations described in Section 2.1 are calculated with data output time steps of 20 yr (the physical time step is even much smaller, of the order of several weeks), thus the time evolution of all quantities given by the simulations are output on grids with 2617–47, 554 points for the models considered in this paper, which range in duration from 52, 340 to 951, 080 yr (Section 5.3). However, due to technical limitations, the radiative transfer models are limited to ∼500–600 time steps per model in order to be run in a reasonable amount of time. Therefore, we must resample the simulation output onto much coarser time step grids. As the primary motivation of this study is to evaluate the ability of the Vorobyov & Basu (2010) simulations to resolve the luminosity problem, and the accretion luminosity is dominated by $\dot{M}_s$ since $R_{\rm star}$ is several orders of magnitude smaller than $R_{\rm disk}$ for all but the earliest times, care must be taken to avoid altering the $\dot{M}_s$ distribution.

Our resampling procedure is designed to alter the $\dot{M}_s$ distribution as little as possible by ensuring that all accretion bursts are included in the resampled time steps. For each model, we define a floor in $\dot{M}_s$ that starts a factor of three higher than $\dot{M}_s$ at the moment of the formation of a protostar and declines at approximately the same average slope as $\dot{M}_s$ throughout the duration of the model. We define any duration of time where $\dot{M}_s$ rises above this floor as a burst and combine bursts separated by less than 100 yr into a single burst. After combining closely spaced bursts we are left with between 0 and 97 bursts (Section 5.4). We then edit the burst time steps by hand so that each burst occurs over no more than five time steps, being careful to retain the first and last time steps and also the time step with the maximum $\dot{M}_s$ so that the total duration and amplitude of each burst is preserved. Finally, we sample the original time steps every N years, where N ranges from 500 to 4000 for the different models and is chosen such that the final number of resampled time steps does not exceed ∼500–600. The final time step grid is then constructed by combining the burst time steps and regularly sampled time steps, eliminating duplicate time steps included both from the bursts and the regular sampling.

Figure 15 shows an example of the resampling for Model 3. The left panel of this figure plots in black $\dot{M}_s$ versus time for the original time steps given by the simulation, whereas the right panel plots $\dot{M}_s$ versus time after resampling the time steps following the procedure described above. Also plotted in each panel are the $\dot{M}_s$ floor used to define bursts (solid gray line) and, for comparison, the constant accretion rate from the core onto the protostar+disk system of $4.57 \times 10^{-6} M_\odot$ yr^{-1} from Paper II (dashed gray line). Comparing the two panels shows that both the number and amplitude of the accretion bursts are preserved, as is the general decline in $\dot{M}_s$ with time.

Careful inspection of Figure 15 shows that not all features of the evolution of $\dot{M}_s$ with time are preserved. In particular, the episodes of lowest $\dot{M}_s$ are not always preserved by the resampling procedure, with the most prominent case occurring at ∼0.12 Myr in the above example. This is a natural result of our adopted procedure since no special effort is devoted to preserving these episodes, thus they will only appear in the resampled time steps if they happen to occur at a time step included by the regular sampling.

To examine the overall effects of resampling on our results, Figure 16 plots histograms of the fraction of total time the models spend in various $\dot{M}_s$ bins for the original (solid, shaded histogram) and resampled (dashed histogram) time steps. The fraction of total time spent in each bin is calculated by dividing the total time spent in each bin (weighted by mass as described above in Section 4) by the total duration of the models (again weighted by mass), with the equation

$$f_{\rm bin} = \frac{\sum_{\rm mass} t_{\rm bin} w_{\rm mass}}{\sum_{\rm mass} t_{\rm collapse} w_{\rm mass}}, \quad \text{(A1)}$$

where $t_{\rm bin}$ is the total time each model spends in the bin, $t_{\rm collapse}$ is the total duration of each model, and $w_{\rm mass}$ is the weight for each model depending on the final stellar mass produced (see

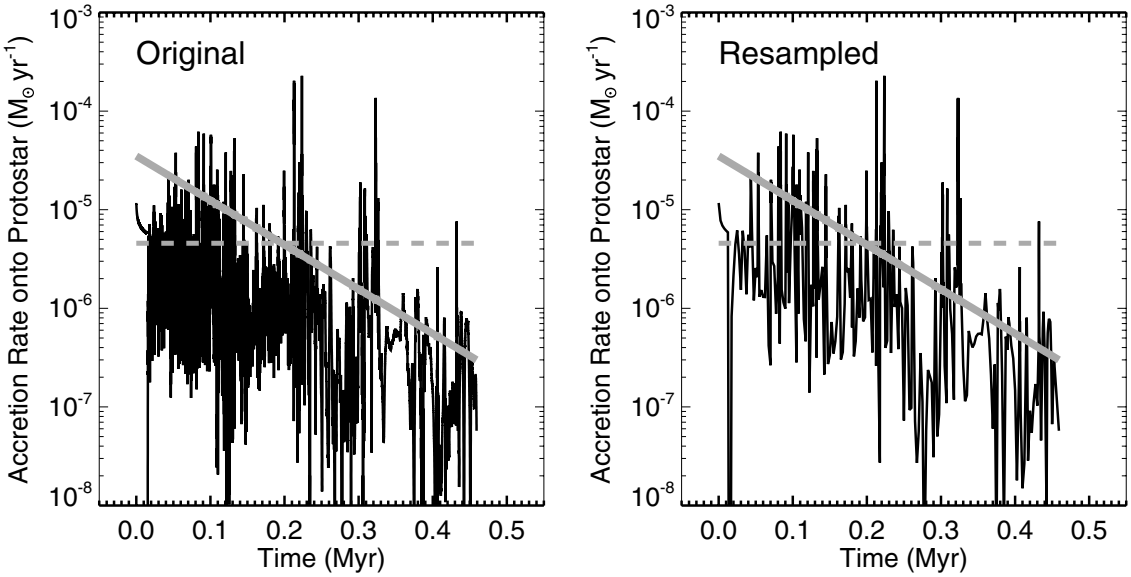

Figure 15. $\dot{M}_s$ vs. time for the original (left) and resampled (right) time steps for model 3. In each panel the black line plots the $\dot{M}_s$ given by the simulation, the solid gray line plots the $\dot{M}_s$ floor used to define bursts, and the dashed gray line plots, for comparison, the constant accretion rate from the core onto the protostar+disk system of $4.57 \times 10^{-6}\ M_\odot\ \mathrm{yr}^{-1}$ from Paper II.

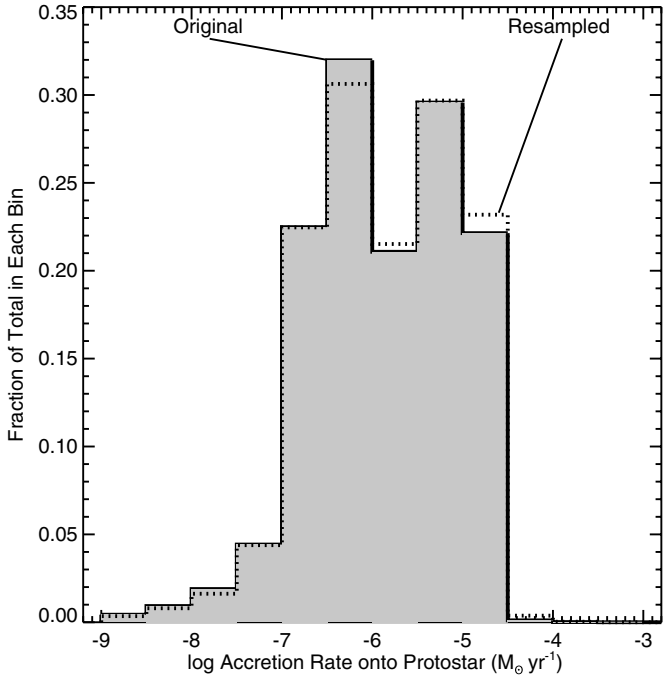

Figure 16. Histograms showing the fraction of total time spent in various $\dot{M}_s$ bins for the original (solid, shaded histogram) and resampled (dashed histogram) time steps. The bin size is 1/2 dex in $\dot{M}_s$.

Section 4). Figure 16 shows that the original and resampled $\dot{M}_s$ distributions are quite similar. There is a very small shift to higher values of $\dot{M}_s$ after resampling seen in a careful inspection of the figure. The models spend 0.5% less time at $\dot{M}_s \leqslant 10^{-7}\ M_\odot\ \mathrm{yr}^{-1}$ and 1.3% more time at $\dot{M}_s \geqslant 10^{-5}\ M_\odot\ \mathrm{yr}^{-1}$ after resampling. This small shift is a result of missing some of the lowest episodes of $\dot{M}_s$ and has a negligible impact on the final luminosity distribution presented in Section 4 since time steps with extremely low values of $\dot{M}_s$ will have their total luminosity dominated by photosphere and external luminosity anyway. We thus conclude that resampling to coarser time step grids, as required by the radiative transfer models, does not fundamentally alter or bias any of the conclusions of this paper.

REFERENCES

Ábrahám, P., Kóspál, Á., Csizmadia, S., et al. 2004, A&A, 419, L39
Acosta-Pulido, J. A., Kun, M., Ábrahám, P., et al. 2007, AJ, 133, 2020
Adams, F. C., & Shu, F. H. 1986, ApJ, 308, 836
Alexander, D. R., Augason, G. C., & Johnson, H. R. 1989, ApJ, 345, 1014
Alves, J., Lombardi, M., & Lada, C. J. 2007, A&A, 462, L17
André, P., Motte, F., & Bacmann, A. 1999, ApJ, 513, L57
André, P., Ward-Thompson, D., & Barsony, M. 1993, ApJ, 406, 122
Armitage, P. J. 2011, ARA&A , 49, 195
Armitage, P. J., Livio, M., & Pringle, J. E. 2001, MNRAS, 324, 705
Aspin, C., Reipurth, B., Beck, T. L., et al. 2009, ApJ, 692, L67
Baraffe, I., Chabrier, G., & Gallardo, J. 2009, ApJ, 702, L27
Basu, S. 1997, ApJ, 485, 240
Basu, S., & Vorobyov, E. I. 2011, ApJ, in revision
Bate, M. 2009, MNRAS, 392, 590
Beichman, C. A., Myers, P. C., Emerson, J. P., et al. 1986, ApJ, 307, 337
Bell, K. R., & Lin, D. N. C. 1994, ApJ, 427, 987
Black, J. H. 1994, in ASP Conf. Ser. 58, The First Symposium on the Infrared Cirrus and Diffuse Interstellar Clouds, ed. R. M. Cutri & W. B. Latter (San Francisco, CA: ASP), 355
Bonnell, I., & Bastien, P. 1992, ApJ, 401, L31
Boss, A. P. 2002, ApJ, 576, 462
Boss, A. P., & Hartmann, L. W. 2001, ApJ, 562, 842
Bourke, T. L., Myers, P. C., Evans, N. J., II, et al. 2006, ApJ, 649, L37
Caratti o Garatti, A., Garcia Lopez, R., Scholz, A., et al. 2011, A&A, 526, L1
Caselli, P., Benson, P. J., Myers, P. C., & Tafalla, M. 2002, ApJ, 572, 238
Cha, S.-H., & Nayakshin, S. 2011, MNRAS, 415, 3319
Chen, H., Myers, P. C., Ladd, E. F., & Wood, D. O. S. 1995, ApJ, 445, 377
Chen, X., Arce, H. G., Zhang, Q., et al. 2010, ApJ, 715, 1344
Cieza, L. A., Kessler-Silacci, J. E., Jaffe, D. T., Harvey, P. M., & Evans, N. J., II. 2005, ApJ, 635, 422
Clarke, C. J. 2009, MNRAS, 396, 1066
Covey, K. R., Hillenbrand, L. A., Miller, A. A., et al. 2011, AJ, 141, 40
D'Antona, F., & Mazzitelli, I. 1994, ApJS, 90, 467
Dapp, W. B., & Basu, S. 2009, MNRAS, 395, 1092
Devine, D., Bally, J., Chiriboga, D., & Smart, K. 2009, AJ, 137, 3993
Di Francesco, J., Evans., N. J., II, Caselli, P., et al. 2007, in Protostars and Planets V, ed. B. Reipurth, D. Jewitt, & K. Keil (Tucson, AZ: Univ. Arizona Press), 17
Draine, B. T. 1978, ApJS, 36, 595
Draine, B. T., & Lee, H. M. 1984, ApJ, 285, 89
Dullemond, C. P., & Dominik, C. 2004, A&A, 417, 159
Dullemond, C. P., & Turolla, R. 2000, A&A, 360, 1187

Dunham, M. M., Chen, X., Arce, H. G., et al. 2011, ApJ, 742, 1
Dunham, M. M., Crapsi, A., Evans, N. J., II, et al. 2008, ApJS, 179, 249
Dunham, M. M., Evans, N. J., II, Bourke, T. L., et al. 2006, ApJ, 651, 945
Dunham, M. M., Evans, N. J., Bourke, T. L., et al. 2010a, ApJ, 721, 995
Dunham, M. M., Evans, N. J., II, Terebey, S., Dullemond, C. P., & Young, C. H. 2010b, ApJ, 710, 470 (Paper II)
Enoch, M. L., Corder, S., Dunham, M. M., & Duchêne, G. 2009a, ApJ, 707, 103
Enoch, M. L., Evans, N. J., II, Sargent, A. I., et al. 2008, ApJ, 684, 1240
Enoch, M. L., Evans, N. J., II, Sargent, A. I., & Glenn, J. 2009b, ApJ, 692, 973
Enoch, M. L., Lee, J.-E., Harvey, P., Dunham, M. M., & Schnee, S. 2010, ApJ, 722, L33
Evans, N. J., II, Allen, L. E., Blake, G. A., et al. 2003, PASP, 115, 965
Evans, N. J., II, Dunham, M. M., Jørgensen, J. K., et al. 2009, ApJS, 181, 321
Evans, N. J., II, Rawlings, J. M. C., Shirley, Y. L., & Mundy, L. G. 2001, ApJ, 557, 193
Fatuzzo, M., Adams, F. C., & Myers, P. C. 2004, ApJ, 615, 813
Fedele, D., van den Ancker, M. E., Petr-Gotzens, M. G., & Rafanelli, P. 2007, A&A, 472, 207
Foster, P. N., & Chevalier, R. A. 1993, ApJ, 416, 303
Furlan, E., Luhman, K. L., Espaillat, C., et al. 2011, ApJS, 195, 3
Galli, D., & Shu, F. H. 1993a, ApJ, 417, 220
Galli, D., & Shu, F. H. 1993b, ApJ, 417, 243
Goodman, A. A., Benson, P. J., Fuller, G. A., & Myers, P. C. 1993, ApJ, 406, 528
Gutermuth, R. A., Bourke, T. L., Allen, L. E., et al. 2008, ApJ, 673, L151
Hartmann, L., & Kenyon, S. J. 1985, ApJ, 299, 462
Hartmann, L., Zhu, Z., & Calvet, N. 2011, arXiv:1106.3343
Hatchell, J., & Fuller, G. A. 2008, A&A, 482, 855
Heiderman, A., Evans, N. J., II, Allen, L. E., Huard, T., & Heyer, M. 2010, ApJ, 723, 1019
Henriksen, R., Andre, P., & Bontemps, S. 1997, A&A, 323, 549
Herczeg, G. J., Karska, A., Bruderer, S., et al. 2011, A&A, submitted (arXiv:1111.0774)
Hosokawa, T., Offner, S. S. R., & Krumholz, M. R. 2011, ApJ, 738, 140
Hunter, C. 1977, ApJ, 218, 834
Johnson, B. M., & Gammie, C. F. 2003, ApJ, 597, 131
Johnstone, D., & Bally, J. 2006, ApJ, 653, 383
Johnstone, D., Fich, M., Mitchell, G. F., & Moriarty-Schieven, G. 2001, ApJ, 559, 307
Johnstone, D., Wilson, C. D., Moriarty-Schieven, G., et al. 2000, ApJ, 545, 327
Kenyon, S. J., Gomez, M., Marzke, R. O., & Hartmann, L. 1994, AJ, 108, 251
Kenyon, S. J., & Hartmann, L. 1995, ApJS, 101, 117
Kenyon, S. J., Hartmann, L. W., Strom, K. M., & Strom, S. E. 1990, AJ, 99, 869
Kóspál, Á., Ábrahám, P., Acosta-Pulido, J. A., et al. 2011, A&A, 527, A133
Kóspál, Á., Ábrahám, P., Prusti, T., et al. 2007, A&A, 470, 211
Kroupa, P. 2002, Science, 295, 82
Lada, C. J., Lombardi, M., & Alves, J. F. 2010, ApJ, 724, 687
Larson, R. B. 1969, MNRAS, 145, 271
Lee, C.-F., Ho, P. T. P., Palau, A., et al. 2007, ApJ, 670, 1188
Lee, C. W., Bourke, T. L., Myers, P. C., et al. 2009, ApJ, 693, 1290
Lee, J.-E. 2007, J. Korean Astron. Soc., 40, 83
Lee, J.-E., Lee, H.-G., Shinn, J.-H., et al. 2010, ApJ, 709, L74
Li, Z.-Y., & Shu, F. H. 1997, ApJ, 475, 237
Lodato, G., & Clarke, C. J. 2004, MNRAS, 353, 841
Machida, M. N., Inutsuka, S.-i., & Matsumoto, T. 2011, ApJ, 729, 42
Maury, A., Andre, P., Men'shchikov, A., Konyves, V., & Bontemps, S. 2011, A&A, 535, A77
McClure, M. K., Furlan, E., Manoj, P., et al. 2010, ApJS, 188, 75
Merín, B., Brown, J. M., Oliveira, I., et al. 2010, ApJ, 718, 1200
Meru, F., & Bate, M. R. 2010, MNRAS, 406, 2279
Motte, F., Andre, P., & Neri, R. 1998, A&A, 336, 150
Motte, F., André, P., Ward-Thompson, D., & Bontemps, S. 2001, A&A, 372, L41
Myers, P. C. 2010, ApJ, 714, 1280
Myers, P. C., Adams, F. C., Chen, H., & Schaff, E. 1998, ApJ, 492, 703
Myers, P. C., & Ladd, E. F. 1993, ApJ, 413, L47
Nayakshin, S., & Lodato, G. 2011, arXiv:1110.6316
Nutter, D., & Ward-Thompson, D. 2007, MNRAS, 374, 1413
Offner, S. S. R., & McKee, C. F. 2011, ApJ, 736, 53
Ossenkopf, V., & Henning, T. 1994, A&A, 291, 943
Palla, F., & Stahler, S. W. 1991, ApJ, 375, 288
Penston, M. V. 1969, MNRAS, 145, 457
Pfalzner, S., Tackenberg, J., & Steinhausen, M. 2008, A&A, 487, L45
Pineda, J. E., Arce, H. G., Schnee, S., et al. 2011, ApJ, 743, 201
Quanz, S. P., Henning, T., Bouwman, J., et al. 2007, ApJ, 668, 359
Rathborne, J. M., Lada, C. J., Muench, A. A., et al. 2009, ApJ, 699, 742
Sadavoy, S. I., Di Francesco, J., Bontemps, S., et al. 2010, ApJ, 710, 1247
Shakura, N. I., & Sunyaev, R. A. 1973, A&A, 24, 337
Shirley, Y. L., Huard, T. L., Pontoppidan, K. M., et al. 2011, ApJ, 728, 143
Shirley, Y. L., Nordhaus, M. K., Grcevich, J. M., et al. 2005, ApJ, 632, 982
Shu, F. H. 1977, ApJ, 214, 488
Simon, J. B., Hawley, J. F., & Beckwith, K. 2011, ApJ, 730, 94
Simpson, R. J., Nutter, D., & Ward-Thompson, D. 2008, MNRAS, 391, 205
Stamatellos, D., & Whitworth, A. P. 2008, A&A, 480, 879
Stamatellos, D., & Whitworth, A. P. 2009, MNRAS, 400, 1563
Staude, H. J., & Neckel, T. 1991, A&A, 244, L13
Terebey, S., Fich, M., Noriega-Crespo, A., et al. 2009, ApJ, 696, 1918
Terebey, S., Shu, F. H., & Cassen, P. 1984, ApJ, 286, 529 (TSC84)
Tassis, K., & Mouschovias, T. C. 2005, ApJ, 618, 783
Testi, L., & Sargent, A. I. 1998, ApJ, 508, L91
van Kempen, T. A., van Dishoeck, E. F., Salter, D. M., et al. 2009, A&A, 498, 167
Vicente, S. M., & Alves, J. 2005, A&A, 441, 195
Vorobyov, E. I. 2009a, ApJ, 692, 1609
Vorobyov, E. I. 2009b, ApJ, 704, 715
Vorobyov, E. I. 2010, ApJ, 723, 1294
Vorobyov, E. I. 2011, ApJ, 729, 146
Vorobyov, E. I., & Basu, S. 2005a, MNRAS, 360, 675
Vorobyov, E. I., & Basu, S. 2005b, ApJ, 633, L137
Vorobyov, E. I., & Basu, S. 2006, ApJ, 650, 956
Vorobyov, E. I., & Basu, S. 2009a, MNRAS, 393, 822
Vorobyov, E. I., & Basu, S. 2009b, ApJ, 703, 922
Vorobyov, E. I., & Basu, S. 2010, ApJ, 719, 1896
Ward-Thompson, D., André, P., Crutcher, R., et al. 2007a, in Protostars and Planets V, ed. B. Reipurth, D. Jewitt, & K. Keil (Tucson, AZ: Univ. Arizona Press), 33
Ward-Thompson, D., Di Francesco, J., Hatchell, J., et al. 2007b, PASP, 119, 855
Watson, D. M., Bohac, C. J., Hull, C., et al. 2007, Nature, 448, 1026
White, R. J., & Hillenbrand, L. A. 2004, ApJ, 616, 998
Young, C. H., & Evans, N. J., II 2005, ApJ, 627, 293 (Paper I)
Young, C. H., Jørgensen, J. K., Shirley, Y. L., et al. 2004, ApJS, 154, 396
Zhu, Z., Hartmann, L., & Gammie, C. 2009a, ApJ, 694, 1045
Zhu, Z., Hartmann, L., Gammie, C., & McKinney, J. C. 2009b, ApJ, 701, 620
Zhu, Z., Hartmann, L., Gammie, C. F., et al. 2010, ApJ, 713, 1134